

The effects of low temperature and vacuum on the  
fracture behavior of organosilicate thin films

by

Soheil Barakat

A thesis

presented to the University of Waterloo

in fulfillment of the

thesis requirement for the degree of

Master of Applied Science

in

Mechanical Engineering

Waterloo, Ontario, Canada, 2011

© Soheil Barakat 2011

## **AUTHOR'S DECLARATION**

I hereby declare that I am the sole author of this thesis. This is a true copy of the thesis, including any required final revisions, as accepted by my examiners. I understand that my thesis may be made electronically available to the public.

## ABSTRACT

A novel load-displacement sensing instrument has been designed and fabricated to characterize the fracture properties of brittle thin films at low temperature ( $-30\text{ }^{\circ}\text{C}$ ) and pressure ( $1.6\text{e-}4\text{ Pa}$ ). In this study, the instrument was used to investigate the effects of harsh environments on the fracture energies of organosilicate glass (OSG) and silicon carbonitride (SiCN) thin films under four-point bend loading. Experiment results showed that the energy release rates of film stacks are the highest when the environment contains a very low water molecule concentration. This condition can be achieved by purging the testing chamber with pure nitrogen or reducing the chamber pressure to less than  $1\text{ Pa}$ . In contrast, cracks propagated readily along OSG/SiCN interfaces when experiments were performed submerged in de-ionized (DI) water. The effect of low temperature ( $-30\text{ }^{\circ}\text{C}$ ) on thin film fracture was also studied and the results demonstrated that there is no observed degradation of the OSG fracture properties. X-ray photoelectron spectroscopy (XPS) was used to identify the chemical composition of the fracture surfaces. Furthermore, a finite element model was used to investigate the effects on the stress intensity factors at the crack tip of a four-point bend sample when a compliant epoxy layer is present in the film stack.

## ACKNOWLEDGEMENTS

I am greatly indebted to Professor Ting Tsui for mentoring me for the last two years while I completed my MASc. It is due to his wisdom and guidance that I have been able to reach this stage in my academic career. His foresight, encouragement, and criticism served as the backbone upon which this thesis is built and proved invaluable when tackling the various problems that arose along the way.

I am also thankful to have had the knowledge and kindness of Professor Pearl Lee-Sullivan throughout my tenure at the University of Waterloo. She never hesitated to clear space in her busy schedule to share her vast knowledge and provide effective direction.

I am grateful to have had the kind assistance of Dr. Han Li as I began this research. The information that he gave me set me months ahead and provided me with a good foundation of experience to build upon.

Last, but certainly not least, I am blessed with the relentless support of my parents and my brother and sister. They exemplify the unwavering nature of true love and inspire me by example to be the best man that I can be and to rise above the challenges that I face. Without a doubt, the biggest challenge that I will ever face is repaying them for all the sacrifices that they have made for me over the years.

# DEDICATION

I dedicate this thesis to my family for their support, inspiration, and love.

# TABLE OF CONTENTS

Author's Declaration.....	ii
Abstract.....	iii
Acknowledgements.....	iv
Dedication .....	v
Table of Contents.....	vi
List of Tables .....	ix
List of Figures.....	x
Chapter 1 Introduction .....	1
1.1 Low-k Dielectrics in Microelectronics .....	1
1.2 Environment-Assisted Fracture .....	6
1.3 The Stress Intensity Approach .....	13
1.4 Effects of Porosity on Fracture Properties of Thin Film Dielectrics .....	18
1.5 Effects of Moisture on Fracture Properties of Thin Film Dielectrics .....	19
1.6 Research Objective .....	22
1.7 Outline of Thesis.....	23
Chapter 2 Instrument Design .....	24

2.1 Design Requirements .....	24
2.2 Design Overview .....	25
2.2.1 Lower Chamber .....	28
2.2.2 Motor Mount.....	33
2.2.3 Upper Chamber .....	35
2.2.4 Feedthrough Panel .....	37
2.3 Chamber Compliance.....	39
2.4 Calibration and Stability Testing .....	44
Chapter 3 Experiment Methods .....	49
3.1 Four-Point Bend Technique.....	49
3.2 Sample Fabrication .....	53
3.3 Thermal-Mechanical Properties of Epotek 353ND Epoxy.....	55
3.4 Finite Element Methods.....	58
3.5 Crack Interface Identification by XPS .....	65
Chapter 4 Results and Discussion.....	68
4.1 Humidity Effects on OSG/SiCN Thin Film Fracture Strength.....	68
4.2 Fracture Strength in Harsh Environments.....	81

Chapter 5 Conclusions .....	87
Appendices.....	89
Appendix A. Photographs of the Test Instrument .....	90
Appendix B. Graphic User Interface .....	95
Bibliography .....	97

## LIST OF TABLES

Table 1.1 Stress Fields Ahead of a Crack Tip under Mode I and Mode II Loading for a Linear Elastic and Isotropic Material. ....	15
Table 2.1 Load-displacement design requirements .....	24
Table 2.2 Environment design requirements .....	25
Table 2.3 List of feedthroughs .....	37
Table 4.1a Testing conditions and results of OSG_1/SiCN film stacks .....	72
Table 4.1b Testing conditions and results of OSG_2/SiCN film stacks.....	72
Table 4.1c Testing conditions and results of OSG_3/SiCN film stack.....	73
Table 4.2a Elemental compositions of fractured OSG_1/SiCN thin film stacks.....	79
Table 4.2b Elemental compositions of fractured OSG_2/SiCN thin film stacks .....	79
Table 4.2c Elemental compositions of fractured OSG_3/SiCN thin film stacks.....	80

# LIST OF FIGURES

Figure 1.1 FTIR measurements of OSG thin films identified the following building blocks: a) $(\text{CH}_3)_{2x}\text{SiO}_{2-x}$ , b) $\text{Si}(\text{CH}_2)\text{O}$ , c) $\text{SiO}_2$ , d) $\text{Si}(\text{CH}_2)_{0.5}\text{O}_{1.5}$ , and e) $\text{H}_{2m}\text{SiO}_{2-m}$ .....	4
Figure 1.2 Dielectric constant of OSG thin films as a function of porosity .....	5
Figure 1.3 Graph of crack velocity vs. energy release rate.....	9
Figure 1.4 Parameters for definition of a crack through the stress intensity approach.....	14
Figure 1.5 Schematic relationship between phase angle and energy release rate.....	17
Figure 2.1 Section view of the mechanical tester constructed for this research .....	27
Figure 2.2 Detailed drawing of the lower chamber section .....	29
Figure 2.3 Four-point bend components inside the chamber.....	31
Figure 2.4 The datum tool with a sample and the loading block (Left) and the datum tool positioning the sample and loading block on top of the pins (Right) .....	32
Figure 2.5 Detailed drawing of the motor mount plate.....	34
Figure 2.6 Detailed drawing of the top chamber section .....	36
Figure 2.7 Detailed drawing of the feedthrough panel .....	38
Figure 2.8 Strain in the motor mount plate as a result of a 20N reaction force applied to the mounting location of the linear actuator .....	41

Figure 2.9 Strain in the lower chamber as a result of a 20N reaction force applied to the mounting location of the motor mount plate.....	42
Figure 2.10 Strain of the test instrument from zero to maximum loading.....	43
Figure 2.11 Stability of the load cell under static loading conditions for ~ 4 hours.....	45
Figure 2.12 Load-displacement curve of a glass slide measured at -30 °C and 20 °C . The linearity and slope of the reading has not been impacted by the change in temperature.....	46
Figure 2.13 Temperature stability of the environment chamber is shown over a 60 minute time frame during which a total fluctuation of 1 °C occurs.....	48
Figure 3.1 Thin film fracture specimen in four point bend configuration .....	51
Figure 3.2 Load-displacement curve of a typical OSG/SiCN film stack. Initially, elastic deformation occurs. The sharp drop in load (near 80 μm displacement) corresponds to pre-crack propagation to the surface of interest.....	52
Figure 3.3 Film Stack Diagram (Not to scale).....	54
Figure 3.4 Load-displacement curves of an epoxy beam at 23 °C, 0 °C, -20 °C, and -40 °C.....	56
Figure 3.5 DMA results showing the change in the storage modulus of the EPOTEK 353ND epoxy.....	57
Figure 3.6 Geometry of the finite element model.....	60
Figure 3.7 Finite element model of the four-point bend sample shown before and after deformation (top), close-ups of the mesh structure (bottom) .....	61

Figure 3.8 J-integral convergence study .....62

Figure 3.9 Phase angle as a function of epoxy layer thickness for two different elastic moduli...64

Figure 3.10 Sample gently broken along score mark to reveal the fracture surfaces for subsequent XPS .....66

Figure 3.11 Spectra of SiCN (top left), OSG\_1 (top right), interfacial surface OSG\_1/SiCN (bottom).....67

Figure 4.1 Energy release rate of OSG/SiCN film stacks as a function of  $\ln(\text{water vapor partial pressure})$ . Also included are specimens tested in DI water and in a nitrogen environment. ....70

Figure 4.2 Energy release rate of OSG films as a function of porosity (%) showing a downward trend with increasing porosity.....71

Figure 4.3 XPS spectra of OSG\_1 samples tested in DI water (top left), air with 70% RH (top right), and pure nitrogen (bottom) .....76

Figure 4.4 XPS spectra of OSG\_2 samples tested in DI water (top left), air with 20% RH (top right), and pure nitrogen (bottom) .....77

Figure 4.5 XPS spectra of OSG\_3 samples tested in DI water (top left), air with 17% RH (top right), air with 5% RH (bottom left), and pure nitrogen (bottom right).....78

Figure 4.6 Harsh environment performance of OSG\_2.....82

Figure 4.7 Harsh environment performance of OSG\_3.....83

Figure 4.8 XPS spectra of OSG\_2 samples tested at -30 °C and 0.46 Pa air (top left), and 20 °C and 1.6e-4 Pa air (top right) .....85

Figure 4.9 XPS spectra of OSG\_3 samples tested at -30 °C and 0.46 Pa air (top left), 20 °C and 0.46 Pa air (top right), and 20 °C and 1.4e-4 Pa air (bottom left).....86

# CHAPTER 1 INTRODUCTION

## 1.1 LOW-K DIELECTRICS IN MICROELECTRONICS

In accordance with Moore's law, CMOS technology has pushed the number of transistors on ultra-large scale integrated circuits (IC's) to the billions and miniaturization limits beyond the ninety nanometer technology node. Due to the signal integration required by the number of active elements, many IC's feature up to eight layers of metal interconnects. These three-dimensional structures are encased by a dielectric material which must provide support during mechanical, thermal, and electrical loading. Furthermore, it must act as a chemical barrier to diffusion of reactive species between the lines and from the surroundings [1]. Inherent parasitic capacitance and resistance of interconnections have become a major limiting factor in the speed of high performance IC's as miniaturization has increased [2]. This has led to the movement away from aluminum interconnect material and silicon dioxide dielectric material to copper metal and low-k dielectrics. Copper has a smaller resistance than traditional interconnect lines while novel interline dielectric materials, low-k materials ( $k < 4$ ), are needed to minimize power requirement of circuits, minimize the capacitance between lines and ground planes, and prevent fringes from laterally extending from lines. Inter-line capacitance is governed by the following relationship:

$$C \approx \frac{k}{d} \quad (1).$$

According to Equation (1), capacitive cross-talk can be reduced by decreasing the interlayer dielectric constant ( $k$ ) and by increasing the distance between lines. Since the semiconductor

industry aims to increase chip density and response times, it is clear that increasing the inter-line distance is not an option; consequently, the only approach is to develop materials with decreasing dielectric constants. Commonly, these materials are porous and contain organic components which define their thermal and/or mechanical properties as compared to traditional SiO<sub>2</sub> dielectrics. A successful low-k dielectric material must endure a multitude of processing steps including dual-damascene lithography, etching, stripping, cleaning, chemical mechanical polishing (CMP), and packaging. Since the ILD is a structural frame with which multi-layer-damascene-stacks are fabricated, the mechanical and thermal reliability of the device created is directly affected by the properties of the material selected. For example, the CMP process exposes the stack to high shear forces and any flaws at the interfaces or in the low-k film can lead to crack initiation and severely impact long-term reliability [3]. Additionally, stress concentrations created by packaging at the corners and edges of IC's are a major point of concern for delamination [4].

Porous silicates are thin films of amorphous silicon-dioxide; however, some of their bridging oxygen atoms are replaced with hydrogen or hydroxyl groups, and by methyl (-CH<sub>3</sub>) or methylene (-CH<sub>2</sub>) organic groups. These hybrid organic-inorganic materials are often referred to as organosilicate glass (OSG). Fourier transform infrared (FTIR) measurements conducted by Lin et al. [5] showed that these films are comprised of five building blocks which are shown in Figure 1.1. The formulae representing the functional groups are as follows: (CH<sub>3</sub>)<sub>2x</sub>SiO<sub>2-x</sub>, Si(CH<sub>2</sub>)O, SiO<sub>2</sub>, Si(CH<sub>2</sub>)<sub>0.5</sub>O<sub>1.5</sub>, and H<sub>2m</sub>SiO<sub>2-m</sub>. The aforementioned formulae represent the proportion of atoms present in each group and x and m are constants determined by relative peaks in FTIR spectra. To further reduce the dielectric constant of the OSG and achieve values as low as k~2.6 to 2.3, nanometer scale pores are often introduced into the matrix with the

porosity in the range of ~7% to ~45% [6-9]. Figure 1.2 shows the relation between porosity and dielectric constant in OSG thin films [9]. In a well hermetically sealed IC product with a protective overcoat such as silicon nitride, these nano-pores are evacuated with the internal pressure defined by the deposition steps during the IC manufacturing processes. The increase in porosity within the OSG molecular structure reduces the average bond density and weakens the mechanical strength of these materials, thereby increasing their vulnerability to stress corrosion cracking. The impact of the reduced mechanical strength of these films may be most pronounced in extreme conditions such as low temperature environments where thermal expansion coefficient mismatch is greatest.

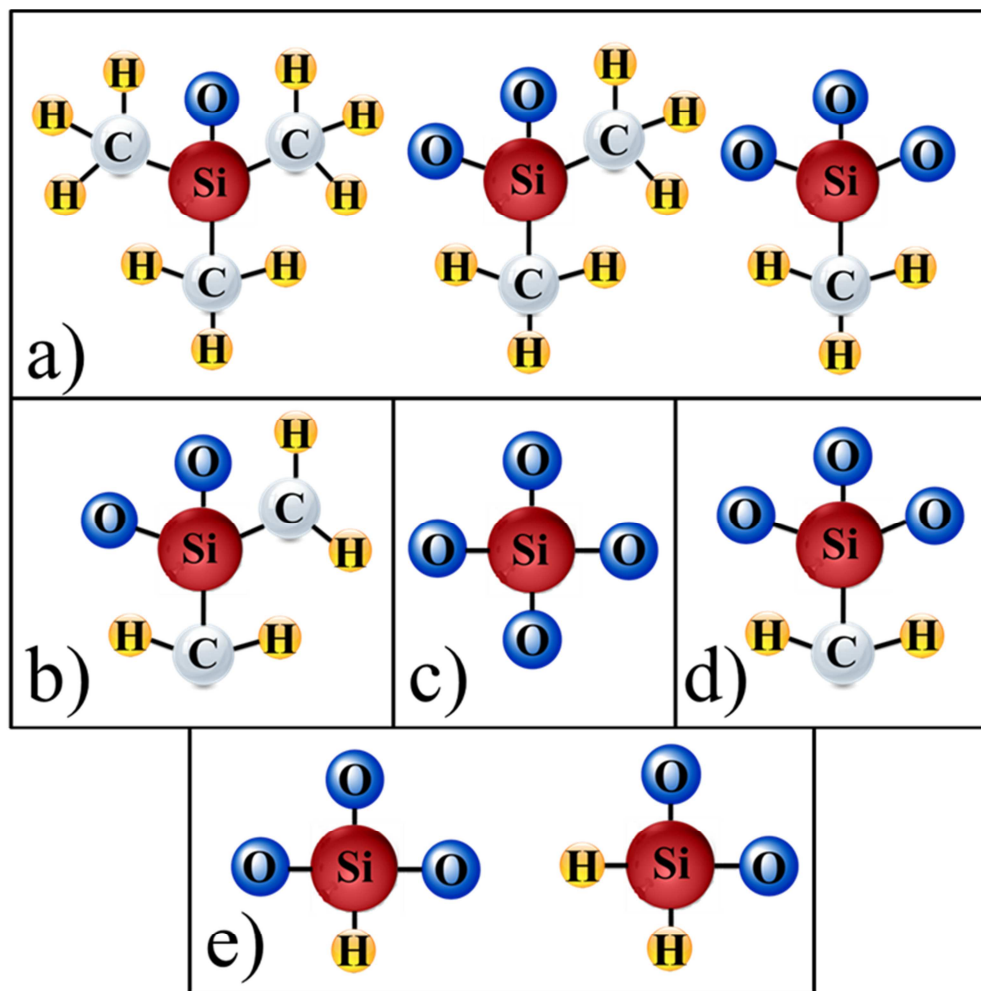


Figure 1.1. FTIR measurements of OSG thin films identified the following building blocks: a)  $(\text{CH}_3)_{2x}\text{SiO}_{2-x}$ , b)  $\text{Si}(\text{CH}_2)\text{O}$ , c)  $\text{SiO}_2$ , d)  $\text{Si}(\text{CH}_2)_{0.5}\text{O}_{1.5}$ , and e)  $\text{H}_{2m}\text{SiO}_{2-m}$ .

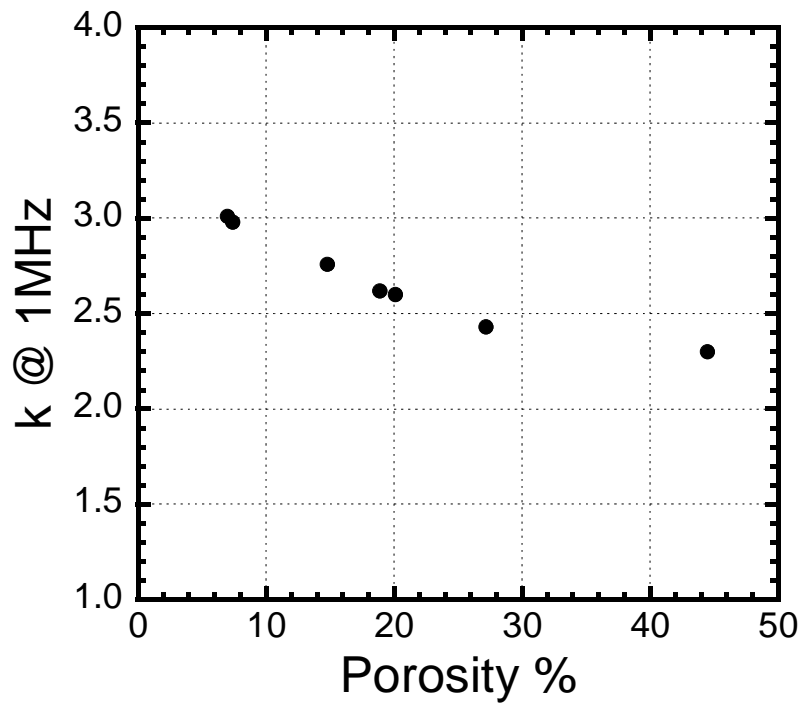
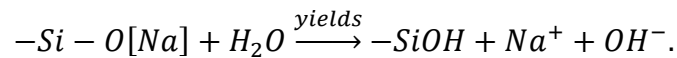


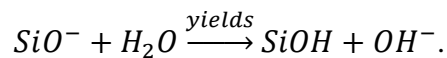
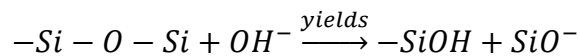
Figure 1.2. Dielectric constant of OSG thin films as a function of porosity [9].

## 1.2 ENVIRONMENT-ASSISTED FRACTURE

Brittle solids undergo environment-assisted cracking as a result of the interaction between reactive species in the environment and highly stressed bonds at a crack tip. The adsorption of water or other reactive molecules weakens bonds at the crack tip which are already stressed by the applied load. Chemisorption causes bonds to rupture in accordance to several models that have been developed [10-15]. Environmental effects on the fracture properties of bulk glass materials such as amorphous silica and borosilicate glass have been thoroughly studied [11, 13, 16-21]. Charles highlighted that the dissolution of silica glass in water vapor is an autocatalytic reaction beginning at the terminal structures [16] as shown:



In a hydrolysis reaction, an oxygen-sodium bond is broken, and the oxygen dissociates a water molecule to bond to a hydrogen ion. This creates a free hydroxyl ion which allows the next step of the dissolution process to proceed as follows:



His experimentation involved four-point bend testing of glass rods using a dead weight in a temperature range of -170 °C to 242 °C at atmospheric pressure. An autoclave was used for high temperature tests while a liquid nitrogen cooled device was used for cold temperatures. He reported that at the lower limit of temperature, delayed fracture is not observed which may be attributed to the starvation of reactive gaseous species. Lawn, using the kinetic gas theory, proposed a two-step diffusion reaction model for molecular flow along a fracture interface. This

model is used to describe environment-assisted fracture in the presence of reactive gases. Furthermore, he developed a theory of atomic crack growth to account for the non-linearity inherent in rupturing of bonds. Wiederhorn used double-cantilever cleavage technique on glass microscope slides by introducing a crack in the mid-plane and applying static loading conditions to the ends. He used this technique to identify the fracture surface energy of glass. He characterized the effect of pH [20], humidity from zero to 100% [13], temperature from 0 to 700 °C [19, 21], vacuum down to 1 mPa [21], and high pressure up to 20 GPa [22] on the fracture properties of glass. He applied a reaction rate controlled model of brittle fracture by Charles and Hillig [15] to predict crack growth velocity in the presence of reactive species [13].

Figure 1.3 shows a characteristic subcritical fracture curve by plotting crack velocity against energy release rate. Based on the application of driving force, three rate-limiting regimes control the rate of crack propagation through the material [11-14, 23]. There is often a force threshold driving force below which crack growth does not occur. After this threshold is surpassed, cracking occurs according to the applied stress intensity via a stress-dependent chemical interaction. The concentration of reactive molecules in the environment has a large impact on crack velocity and can shift the graph vertically for a given stress intensity value; therefore, it is called the reaction-controlled regime. If the applied force is increased further, a plateau occurs where crack velocity is only minimally affected by the applied energy release rate. In this state, known as the transport limited regime, crack velocity is limited by the transport of reactive species such as water to the crack tip. If applied stress intensity is further increased, then catastrophic failure occurs at which point fracture rate is no longer dependent on the environment. To further understand environment-assisted cracking, consider a reaction occurring on the surface of a material as separated into the following steps: (1) Transport of reactants to the

surface, (2) reactant adsorption, (3) surface reaction, (4) product desorption, and (5) transport of products away from the surface [14, 24]. Since the reaction products are left behind as new crack surfaces are uncovered, stages 4 and 5 can be disregarded as factors impacting reaction rate. Step 2 may be further separated into Van der Waals adsorption and chemisorption. Since chemisorption is a chemical reaction, it has the potential to limit fracture progress. This leaves diffusion, chemisorption, and chemical reaction as the rate limiting steps of a surface reaction. The rate of chemisorption and chemical reaction depend on the stress state of the bonds at the crack tip; therefore, it is reasonable to attribute the reaction-controlled regime to be governed by these processes. Diffusion, on the other hand, is not dependent on applied load. This means that diffusion is the principal factor which creates the transport controlled regime.

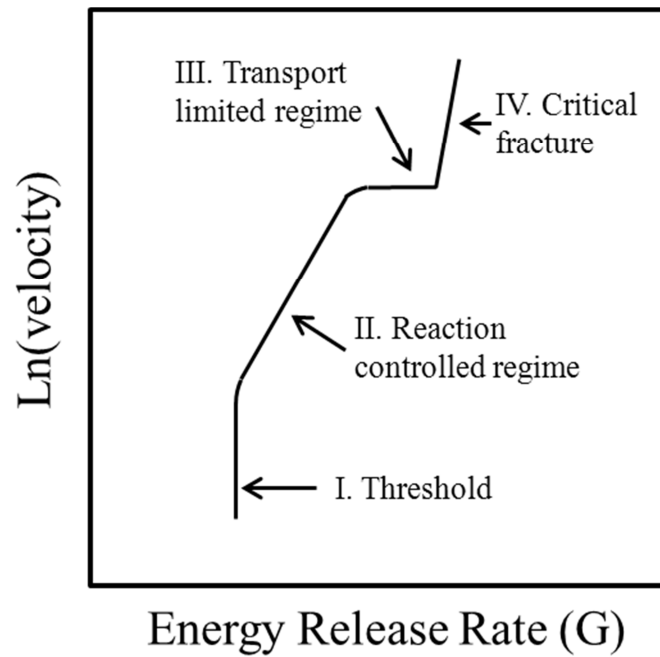


**Figure 1.3. Graph of crack velocity vs. energy release rate.**

Based on the energies of kink configuration as explained by Lawn, the frequencies of bond rupture and healing in a reactive environment are impacted by the mechanical energy release rate. As defined by the Griffith's criterion [25], the total energy of a quasi-static crack system can be written as

$$U = (-W_L + U_E) + U_S \quad (2)$$

where  $W_L$  is the work of the applied force,  $U_E$  is the strain energy, and  $U_S$  is the surface energy. In order for this energy balance to be upheld, as a crack extends, the surface energy must increase. This leads to the following formulation that describes a change in energy with  $A$  as the crack area:

$$\frac{dU}{dA} = \frac{d(-W_L + U_E)}{dA} + \frac{dU_S}{dA} = -G + 2\gamma \quad (3).$$

In Equation (3),  $G$  is the mechanical energy release rate and  $\gamma$  is the surface energy. The assumption is made that  $G$  is applied distal to the crack tip and may be considered continuous. Also, the surface energy is expected to oscillate in accordance with the periodicity of the atomic bonds. An increase in crack area  $A$  can be modeled by

$$A = \frac{f}{N} \quad (4)$$

where  $f$  is the net rupture frequency of bonds, and  $N$  is the number of bonds per unit area. If governed by the Maxwell-Boltzmann statistical distributions, the net frequency of bond breakage is given by:

$$f = f_0 \left\{ \exp\left(-\frac{\vec{G}_0^*}{kT}\right) - \exp\left(-\frac{\overleftarrow{G}_0^*}{kT}\right) \right\} \quad (5).$$

In Equation (5),  $\overset{\rightarrow}{G}_0^*$  and  $\overset{\leftarrow}{G}_0^*$  are activation energies for bond rupture and healing respectively,  $f_0$  is the lattice vibration frequency ( $f_0 \approx kT/h$ ),  $k$  is Boltzmann's constant,  $T$  is the absolute temperature, and  $h$  is Planck's constant. Adding the effects of energy release rate to the system, if the energy release is not too large, the energy barriers become:

$$\overset{\rightarrow}{G}^* = \overset{\rightarrow}{G}_0^* - \frac{\beta G}{N}, \quad \overset{\leftarrow}{G}^* = \overset{\leftarrow}{G}_0^* - \frac{(1-\beta)G}{N} \quad (6).$$

Equation (5) then becomes:

$$\begin{aligned} f &= f_0 \left\{ \exp\left(-\frac{\overset{\rightarrow}{G}_0^* \frac{\beta G}{N}}{kT}\right) - \exp\left(-\frac{\overset{\leftarrow}{G}_0^* \frac{(1-\beta)G}{N}}{kT}\right) \right\} \\ &= f_0 \left\{ \exp\left(\frac{\beta G - \gamma}{NkT}\right) - \exp\left(-\frac{(1-\beta)G - \gamma}{NkT}\right) \right\} \times \exp\left(\frac{\overset{\rightarrow}{G}_0^* + \overset{\leftarrow}{G}_0^*}{2kT}\right) \end{aligned} \quad (7).$$

If the energy barrier is symmetric ( $\beta = 1/2$ ), the following relation can be made according to  $\sinh(x) = \frac{1}{2}[\exp(x) - \exp(-x)]$ :

$$f = 2f_0 \exp\left(-\frac{G_a^*}{kT}\right) \sinh\left(\frac{-G+2\gamma}{2NkT}\right) \quad (8).$$

In Equation (8),  $G_a^* = \frac{\overset{\rightarrow}{G}_0^* + \overset{\leftarrow}{G}_0^*}{2}$ . Taking into consideration the distance  $d$  between the bonds, crack velocity can be derived as:

$$\begin{aligned} v &= 2bf_0 \exp\left(-\frac{G_a^*}{kT}\right) \sinh\left(\frac{-G+2\gamma}{2NkT}\right) \\ v &= v_0 \sinh\left(\frac{-G+2\gamma}{2NkT}\right) \end{aligned} \quad (9).$$

In Equation (9),  $v_0$  is a reference velocity. Equation (9) is applicable to environment-assisted cracking in ambient and aqueous settings.

In the case of transport-limited fracture regime, if the crack opening is larger than the mean free path of the gas molecules, the flow of ambient gas can be modeled as continuous flow of a low-viscosity fluid. As the crack tip is approached, there exists a point beyond which molecules will more frequently collide with the crack surfaces than with each other, and transport occurs by molecular flow characteristics. At standard temperature and pressure, the mean free path of air molecules is  $\sim 0.1 \mu\text{m}$  which for the case of a fracture in a brittle solid, corresponds to a distance of  $\sim 1 \text{ mm}$  from the crack tip. This means that molecular flow is the mode of reactant transport to the crack tip, and fracture velocity is defined as

$$v_0 = \frac{64(1-\nu^2)Gp_r}{3\pi nNE\sqrt{2\pi m_r KT} \ln\left(\frac{l}{b}\right)} \quad (10)$$

where  $p_r$  and  $m_r$  are the partial pressure and molar mass of the reactive species  $r$  in the environment respectively,  $l$  is the mean free path, and  $n$  is the number of species adsorbed per bond [11].

### 1.3 THE STRESS INTENSITY APPROACH

Whereas in the previous section fracture is described in terms of energy criterion, it is also sufficient to define cracking using stress intensity. Assuming isotropic linear elastic behavior, with a polar coordinate axis with its origin at the crack tip, the stress field in a cracked body can be described by:

$$\sigma_{ij} = \left(\frac{k}{\sqrt{r}}\right) f_{ij}(\theta) + \sum_{m=0}^{\infty} A_m r^{\frac{m}{2}} g_{ij}^m(\theta) \quad (11).$$

In Equation (11),  $\sigma_{ij}$  is a stress tensor,  $k$  and  $f_{ij}$  are proportionality constants related to load configuration, and  $r$  and  $\theta$  are defined according to Figure 1.4 [26-29]. In the higher order terms,  $A_m$  is amplitude and  $g_{ij}^m$  is a dimensionless function of  $\theta$ . As  $r$  approaches zero, the leading term approaches infinity because of the  $\frac{1}{\sqrt{r}}$  relation and the higher order terms approach zero and can be ignored. There are 3 modes of crack loading: mode I opening, mode II in-plane shear, and mode III out-of-plane shear. Each mode produces a different set of proportionality constants  $k$  and  $f_{ij}$ . Replacing  $k$  with  $K = k\sqrt{2\pi}$ , the stress fields ahead of a crack tip for modes I to III can be defined as follows:

$$\lim_{r \rightarrow 0} \sigma_{ij}^{(I)} = \frac{K_I}{\sqrt{2\pi r}} f_{ij}^{(I)}(\theta) \quad (12)$$

$$\lim_{r \rightarrow 0} \sigma_{ij}^{(II)} = \frac{K_{II}}{\sqrt{2\pi r}} f_{ij}^{(II)}(\theta) \quad (13)$$

$$\lim_{r \rightarrow 0} \sigma_{ij}^{(III)} = \frac{K_{III}}{\sqrt{2\pi r}} f_{ij}^{(III)}(\theta) \quad (14).$$

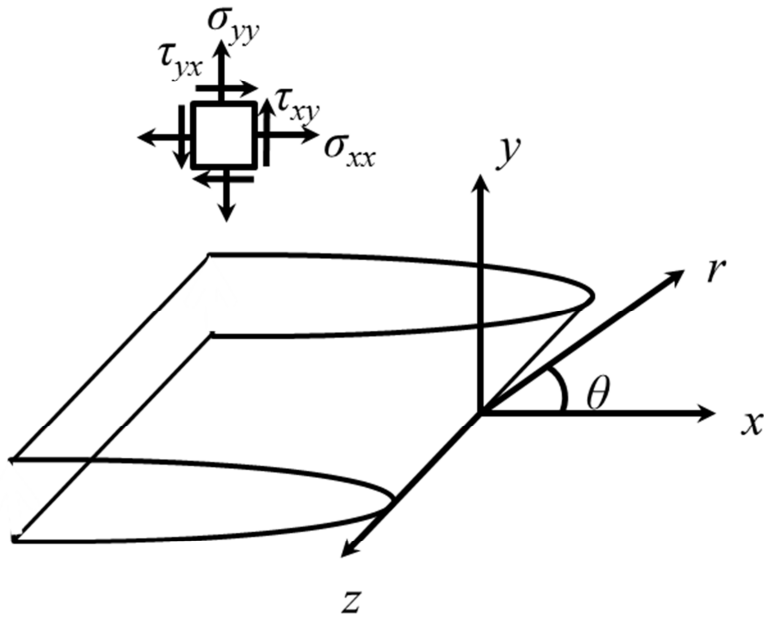


**Figure 1.4. Parameters for definition of a crack through the stress intensity approach.**

Detailed expressions of stress fields are shown in Table 1.

**Table 1.1. Stress fields ahead of a crack tip under mode I and mode II loading for a linear elastic and isotropic material [29].**

	Mode I	Mode II
$\sigma_{xx}$	$\frac{K_I}{\sqrt{2\pi r}} \cos\left(\frac{\theta}{2}\right) \left[1 - \sin\left(\frac{\theta}{2}\right) \sin\left(\frac{3\theta}{2}\right)\right]$	$-\frac{K_{II}}{\sqrt{2\pi r}} \sin\left(\frac{\theta}{2}\right) \left[2 + \cos\left(\frac{\theta}{2}\right) \cos\left(\frac{3\theta}{2}\right)\right]$
$\sigma_{yy}$	$\frac{K_I}{\sqrt{2\pi r}} \cos\left(\frac{\theta}{2}\right) \left[1 + \sin\left(\frac{\theta}{2}\right) \sin\left(\frac{3\theta}{2}\right)\right]$	$\frac{K_{II}}{\sqrt{2\pi r}} \sin\left(\frac{\theta}{2}\right) \cos\left(\frac{\theta}{2}\right) \cos\left(\frac{3\theta}{2}\right)$
$\tau_{xy}$	$\frac{K_I}{\sqrt{2\pi r}} \cos\left(\frac{\theta}{2}\right) \sin\left(\frac{\theta}{2}\right) \cos\left(\frac{3\theta}{2}\right)$	$\frac{K_{II}}{\sqrt{2\pi r}} \cos\left(\frac{\theta}{2}\right) \left[1 - \sin\left(\frac{\theta}{2}\right) \sin\left(\frac{3\theta}{2}\right)\right]$
$\sigma_{zz}$	0 ( <i>Plane Stress</i> ) $\nu(\sigma_{xx} + \sigma_{yy})$ ( <i>Plane Strain</i> )	0 ( <i>Plane Stress</i> ) $\nu(\sigma_{xx} + \sigma_{yy})$ ( <i>Plane Strain</i> )
$\tau_{xz}, \tau_{yz}$	0	0

Considering an exclusively mode I crack field on the crack plane ( $\theta = 0$ ), then  $\sigma_{xx}$  and  $\sigma_{yy}$  are equal and are described by:

$$\sigma_{xx} = \sigma_{yy} = \frac{K_I}{\sqrt{2\pi r}} \quad (15).$$

In Equation (15), the  $\frac{1}{\sqrt{r}}$  singularity dominates the stress field and describes what is known as the singularity dominated zone. The stress intensity factor defines the amplitude of the singularity as well as the stresses, strains, and displacements within the field. For a mixed mode loading configuration as described by stress intensity factors, the contributions from each mode are superimposed in order to define a stress component. The phase angle of loading  $\varphi$  is written as:

$$\varphi = \tan^{-1} \left( \frac{K_{II}}{K_I} \right) \quad (16).$$

So far, fracture has been described by two separate approaches, one involving the energy release rate ( $G$ ) that results from crack extension, and another by ( $K$ ) involving the local stresses, strains, and displacement in the singularity dominated zone at the crack tip. In other words, energy release rate is a global parameter while stress intensity is local. Since these two approaches equally describe fracture, then they must be equivalent. If strain energy release rate is expressed as

$$G = \frac{\pi\sigma^2 a}{E} \quad (17)$$

where  $a = \frac{1}{2}$  crack length and stress intensity is expressed as

$$K_I = \sigma\sqrt{\pi a} \quad (18),$$

the combination of Equations (17) and (18) yields

$$G = \frac{K_I^2}{E} + \frac{K_{II}^2}{E} + \frac{K_{III}^2(1+\nu)}{E} \quad (19).$$

In Equation (19), the elastic modulus for the plane stress case is  $E$  and for the plane strain case is  $\frac{E}{1-\nu^2}$ . Figure 1.5 shows that the energy release rate of a sample increases with phase angle in accordance with the sum of the squared stress intensity factors in Equation (17). In order to understand the effect of the various thin film components, especially the relatively compliant epoxy, on the stress intensity factors during our tests, a simulation in ABAQUS CAE is utilized. Details of the model used are discussed in section 3.4.

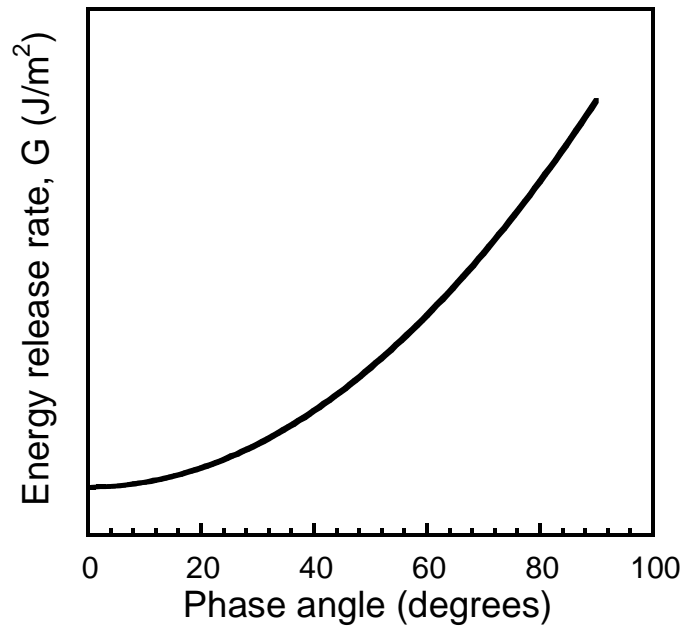


**Figure 1.5. Schematic relationship between phase angle and energy release rate.**

## 1.4 EFFECTS OF POROSITY ON FRACTURE PROPERTIES OF THIN FILM DIELECTRICS

The fracture energy of a series of OSG films deposited with different amounts of porosity in the range of ~7% to ~50% were evaluated by Guyer et al. [30], Lin et al. [31], Li et al. [9], Maidenberg et al. [32], Iacopi et al. [33], and Merrill et al. [34]. The introduction of subtractive porosity into dielectric films degenerates mechanical properties by reducing both the Young's modulus ( $E$ ) and hardness ( $H$ ). FEM simulation of the stresses incurred during damascene processing done by Iacopi et al. indicates that coefficient of thermal expansion (CTE) mismatch between low-k dielectric and barrier materials, high stresses are induced in the barrier film [3]. Due to the presence of the stable organic terminal groups in the structure of dielectric films, they generally exhibit low surface energy and thus have low adhesion values. These attributes, along with the low fracture strength, stack up to make interlayer dielectrics especially vulnerable. In another study, Iacopi et al. showed that thermal activation and UV irradiation of porous OSG films cleaves stable bonds on the surface and increases the film's surface energy as well as cohesive fracture energy [33]. Smith et al. further examined the effect of UV exposure and found that electronic polarizability of their film (25% porosity) steadily decreased due to the loss of methyl groups while ionic polarizability increased. Similar work by Merrill et al. confirms that delamination energy decreases with film porosity and increases with plasticity. Merrill also showed that fracture propagation is dependent upon the mode mix. Maidenberg et al. used 4-PB fracture method to analyze the effect of residue of porogen molecules on the interfacial fracture energy of OSG. This work shows that controlled decomposition of the porogen can result in fracture energy increase by more than one order of magnitude [32]. Guyer et al. show that the mixed mode fracture energy ( $G_p$ ) of porous thin films can be modeled by the following equation:

$$G_p = G_{dense} \left( \frac{\rho_{porous}}{\rho_{dense}} \right)^n \quad (20).$$

In Equation (20)  $\rho_{dense}$  is the density of the dense film and  $\rho_{porous}$  is the density of the porous film and  $n = 2$  [30]. They attributed the non-linearity of this relationship to the mode mixicity inherent in the 4-PB test because pure mode I fracture tests, namely double cantilever beam, showed that fracture strength does indeed scale linearly with porosity. In agreement with the work of Guyer et al., Lin et al. also confirmed that cohesive strength of OSG scales linearly with bond density. They showed that UV irradiation significantly improves the mechanical properties of OSG by increasing network connectivity while having a slight degenerative impact on the dielectric constant. Li et al. showed that the microstructure of OSG must evolve from having isolated pores at high density, to highly interconnected pores at low density. They employed FEM to show that fracture strength decreases linearly as porosity increases based on a planer through-pore fracture regime [9]. Their results show that the energy release rate of these films decreases with increasing porosity.

## **1.5 EFFECTS OF MOISTURE ON FRACTURE PROPERTIES OF THIN FILM DIELECTRICS**

Sparked by integrated circuit mechanical reliability concerns, environment-assisted fracture of thin-film dielectrics has been a topic of interest and moisture and temperature effects have been studied [35-38]. Several experimental techniques have been developed to characterize the fracture strength of thin films, such as, channel cracking [4, 39-41], four-point bend [30, 42-43], and double cantilever beam [9, 31]. The fracture strength of porous OSG and its adhesion properties with different capping materials under different environmental conditions was studied

by Vlassak et al. [42], Tsui et al. [44], Lin et al. [43], Lane et al. [38], and Guyer et al. [45]. Vlassak et al. investigated the subcritical crack growth of OSG films with different capping layers at different relative humidity levels ranging from 0 to 100% at room temperature. They found a linear relationship between the logarithm of water partial pressure and crack velocity at any energy release rate. Furthermore, measurements in aqueous environments showed that an increase in concentration of hydroxyl ions reduces the threshold energy release rate [42]. Tsui et al. looked at the adhesion energy of OSG films to several different capping layers as a function of time submerged under water at 24 °C and at 100 °C. At higher temperature, the rate of reduction of OSG adhesion energy is faster. Generally, Tsui showed that fracture toughness decreases with increasing submersion time and that water reverses the enhancement in mechanical properties by UV irradiation almost completely. Furthermore, after soaking groups of samples in deionized water for different lengths of time, they were tested at different humidity levels. This experiment showed that the impact of the testing environment on adhesion energy is attenuated with longer submersion times. Tsui et al. also showed that annealing the films by vacuum-baking at 250°C for three hours completely reverses the degenerative impact of the submersion process and the OSG film's initial fracture strength returns. This implies that Si-O bonds do not react with water until they are stressed [44]. Further work at room temperature and atmospheric pressure by Lin et al. showed that the preferential path for water diffusion is along OSG/Si interface.

In general, the fracture strength of the OSG in the reaction controlled regime decreases with the amount of reactive species in the surrounding environment. Assuming that water vapor in the environment can be modeled as an ideal gas and the crack propagation rate is in the

reaction controlled regime, the fracture energy ( $G$ ) at a fixed crack velocity is related to the partial pressure of moisture  $p_{H_2O}$  in the environment as

$$G = B - nNRT \ln(p_{H_2O}) = B - A \ln(p_{H_2O}) \text{ for } G \leq G_c \quad (21)$$

where  $n$  is the number water molecule reacting with each broken bond,  $N$  is the bond density,  $R$  is the gas constant, and  $T$  is the absolute temperature of the environment [12, 35, 38, 42-44, 46]. As discussed previously, it is known that the total energy required to separate an interface consists of many energy absorbing processes; however, it is dominated by the energy required to rupture chemical bonds. As a result, even slight changes in barrier/dielectric interfaces due to interactions between crack tip bonds and environmental species may dramatically reduce the amount of energy required for advancement of the crack. Investigating this effect on commonly used Cu interconnect structures, Lane et al. fabricated thin film stacks consisting of  $SiO_2$  with TaN or Ta on silicon substrates and diffusion bonded them together to form 4-PB specimens [38]. Critical and subcritical debonding experiments were conducted inside an environment chamber with controlled temperature and humidity level control (17 °C – 80 °C, 5% - 95% RH). Lane et al. found that at any given moisture level, there is a corrosion threshold which creates a vertical region in the velocity vs. energy release rate (V-G) plot. This is in agreement with the behavior of bulk glasses. It was also observed that for the temperature range investigated, moisture content had a greater impact on fracture energy than temperature. It was demonstrated that there exists a linear relationship between the cohesive strength of these materials and the density of Si-O bonds, and a similar linear relationship between the Si-O bonds and the dielectric constant. As such, it is deduced that both aforementioned properties are controlled by Si-O density. This suggests that as the number of Si-O bonds decreases, the effect of moisture in the environment also decreases. It is notable that for low  $k$  dielectrics, the maximum effective

interfacial strength is limited by the cohesive strength of the material itself. Furthermore, as delamination velocity decreased, a shift in region I of the V-G plot did not occur. Lane et al. attributed this phenomenon on the onset of steric hindrance whereby the fracture geometry inhibits the migration of water molecules to the crack tip. Lane also highlighted that it is important to consider the entire structure when analyzing the susceptibility to cracking – copper pads, for example, contribute to the strain energy released when the upper film cracks.

## **1.6 RESEARCH OBJECTIVE**

The survey of literature shows that virtually all of OSG fracture studies were conducted in ambient temperatures and at atmospheric pressure with very few experiments performed in harsh environments, such as vacuum and at sub-zero temperatures. The fracture properties of these dielectric materials at low-temperature and pressure are very important for IC mechanical reliability. This is because a large amount of shear stress can be generated by the thermal expansion coefficient mismatch between the under-fill packaging materials and the silicon substrate at low temperatures. This stress becomes the driving force for mechanical failure such as BEOL thin film delamination or cracking. As a result, it is vital to characterize the fracture energy of the BEOL structures in these harsh environments. There are two objectives for the current project. The first is to design and construct a load-displacement sensing instrument that can operate in a wide range of pressures with the lowest limit near 0.0001 Pa. This equipment should also be capable of performing experiments near temperature of -170 °C. To fulfill the second objective of this research, this cryogenic thin film mechanical tester is to be fitted with a four-point-bend testing apparatus to characterize the critical fracture strengths of OSG thin films with dielectric values of 2.60, 2.43, and 2.30.

## **1.7 OUTLINE OF THESIS**

This thesis consists of 5 chapters. The second chapter outlines the design process to construct a load and displacement sensing instrument capable of operating in harsh conditions. This chapter also includes a description of the actual performance of the device. The third chapter describes the procedure for fabricating samples with OSG thin film stacks, and techniques used to determine their fracture properties in different environments. Furthermore, a description of the finite element model is provided. The fourth chapter presents OSG fracture results are presented along with detailed discussions. The fifth chapter provides conclusions and proposes future work.

## CHAPTER 2 INSTRUMENT DESIGN

In Chapter 2, the design and fabrication of the test equipment is discussed. The accuracy of the delamination tests relies on the stack-up of the precision of the measurement equipment and the rigidity and stability of the frame. The first goal of this research project is to construct a load-displacement sensing instrument that can operate in a wide range of pressures with the lowest limit near 0.0001 Pa. This equipment should also be capable of performing experiments near the cryogenic temperature of approximately -170 °C.

### 2.1 DESIGN REQUIREMENTS

One objective of this work is to develop a novel load-displacement measurement instrument that can operate in a wide range of pressures with the lowest limit near 0.0001 Pa. This equipment must also be capable of performing experiments near the cryogenic temperature of approximately -170 °C. Table 2.1 shows the requirements of the load-displacement module of the instrument. The main function of this mechanical tester is to characterize the critical fracture

**Table 2.1. Load-displacement design requirements.**

	Range	Tolerance
Force	0-50 N	1% full scale error
Displacement	0-25 mm	1% full scale error
Precision	<50 nm per full step	-

strength of OSG thin films using a four-point bending apparatus. Since the fracture strength of these films under ambient conditions has been well characterized [31, 44-45], some preliminary

load-displacement information is available for design specification. The actual displacement range required for 4-PB testing is less than 5 mm; however, in order to enable this machine to facilitate different test setups, such as double-cantilever beam [9, 31] and pillar compression testing, a range of 25 mm is selected. The environmental requirements are listed in Table 2.2.

**Table 2.2. Environment design requirements.**

	Range
Temperature	-196 °C -30 °C
Pressure	0.0001 Pa -101325 Pa

Liquid nitrogen is a readily available material and its boiling point is selected as the lowest tolerable temperature for the instrument. This means that the case where the entire device with the exception of the vacuum system is submerged in liquid nitrogen must be tolerated and not cause permanent damage to the machine.

## **2.2 DESIGN OVERVIEW**

In focus of the objectives outlined in this work, great emphasis is placed on the low temperature and low pressure performance of the test instrument. For subcritical cracking experiments, samples are initially loaded and then left to unload as subcritical fracture takes place. Based on the fracture velocity, subcritical experiments can take hours to complete, often with small changes in force occurring. This type of test requires very stable conditions. Temperature fluctuations as well as pressure changes result in variations in the size of the chamber and changes in the force reading.

Figure 2.1 shows the cross section of the design of the test mechanism. The vacuum vessel serves multiple functionalities as a loading frame as well as a heat sink. The instrument is comprised of four major components: the lower chamber, the motor mount, the upper chamber, and the feedthrough mount, all of which are further described in the following four sections. As the material of choice, stainless steel 304 (SS 304) is selected because of its material properties. SS 304, a chromium-nickel austenitic steel, has good toughness at low temperature without a steep ductile to brittle transition. This makes it suitable for a low temperature device. Furthermore, it is a commonly used material for vacuum and food technology which means that machining and welding facilities are easily found. For cooling, a well-insulated cage is constructed around the entire instrument. This box is filled with dry ice up to the midway point of the upper chamber, and a lid encloses the cool area. Ambient air is blown onto the feedthrough mount in order to insure that the temperature of the electrical components does not fall below 0 °C. For future low temperature experiments, two copper coils are available as carriers of cooling and heating agent. One copper coil is wrapped around the lower chamber for delivery of liquid nitrogen cooling agent. The other is coiled around the upper chamber for delivery of water to keep electrical components at room temperature. Appendix A shows photographs of the finished test instrument. In order to control the various components in the chamber and run experiments, a graphic user interface is created using National Instruments Labview. Appendix B shows a screenshot of the control program which displays thermocouple values, motor control commands, load cell value, file saving controls, as well as a force versus displacement graph.

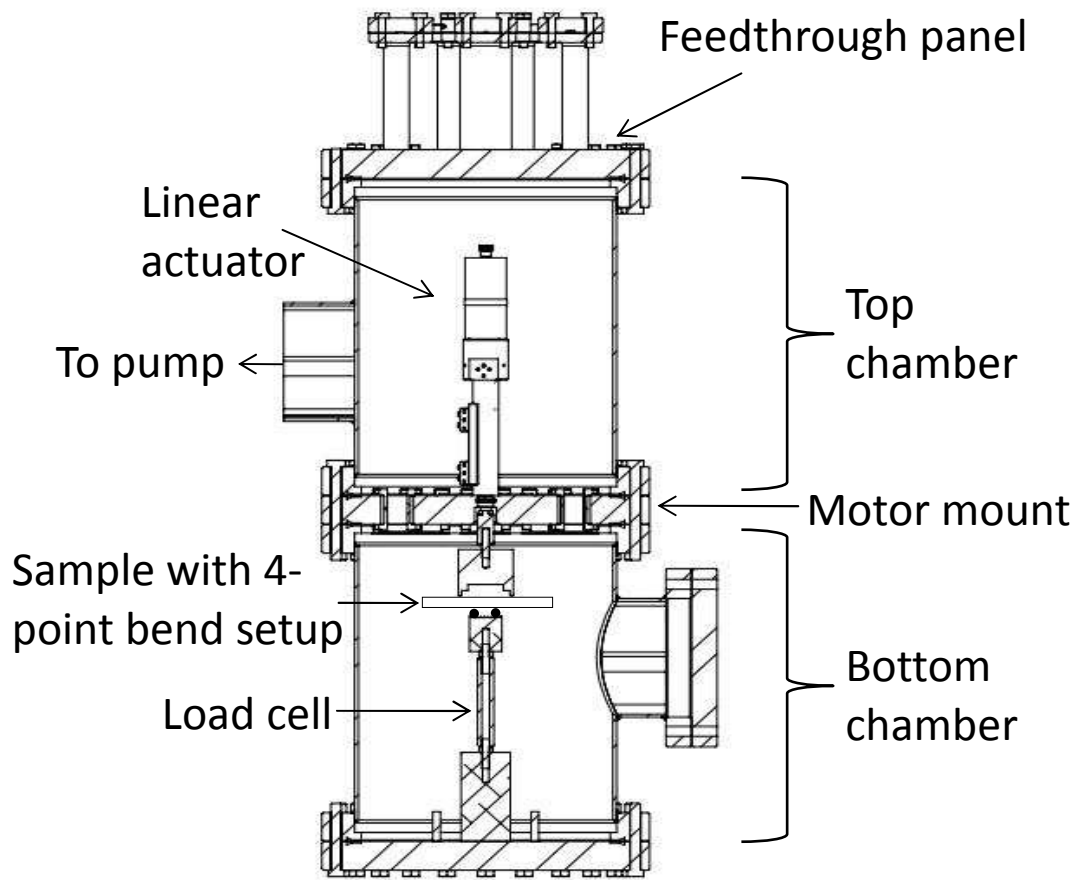


**Figure 2.1. Section view of the mechanical tester constructed for this research.**

### 2.2.1 LOWER CHAMBER

As stated earlier, the bottom section of the chamber serves multiple purposes. In addition to facilitating vacuum, this section is a heat sink as well as a loading frame. Figure 2.2 shows a detailed drawing of this item. It is comprised of an 8” outer diameter pipe with a sidewall thickness of 0.5” and has a 10” ConFlat flange welded to each end for attachment to other vacuum components. The increased thickness of the sidewall is an attempt to minimize the strain that is developed as a sample is loaded during a test. An additional benefit that comes with increased sidewall thickness is the added volume of steel. This improves temperature stabilization because a change in temperature will require more energy output according to the following equation:

$$dQ = mc\Delta T \quad (22).$$

In Equation (22),  $dQ$  is the change in energy,  $m$  is mass,  $c$  is the specific heat capacity (SHC) of the material, and  $\Delta T$  is the change in temperature. The SHC of SS 304 is 500J/kgK [47] which requires that 500 Joules of energy be input into 1 kg of material for a change in temperature of 1 °C. If the mass of the total system increases, then a greater amount of energy must be exchanged for achieving a temperature change. This is a desirable trait because it will attenuate small changes in energy exchange and stabilize temperature. A 4” opening in the side of the main chamber allows access to the test chamber for changing of samples through a 6” ConFlat flange.

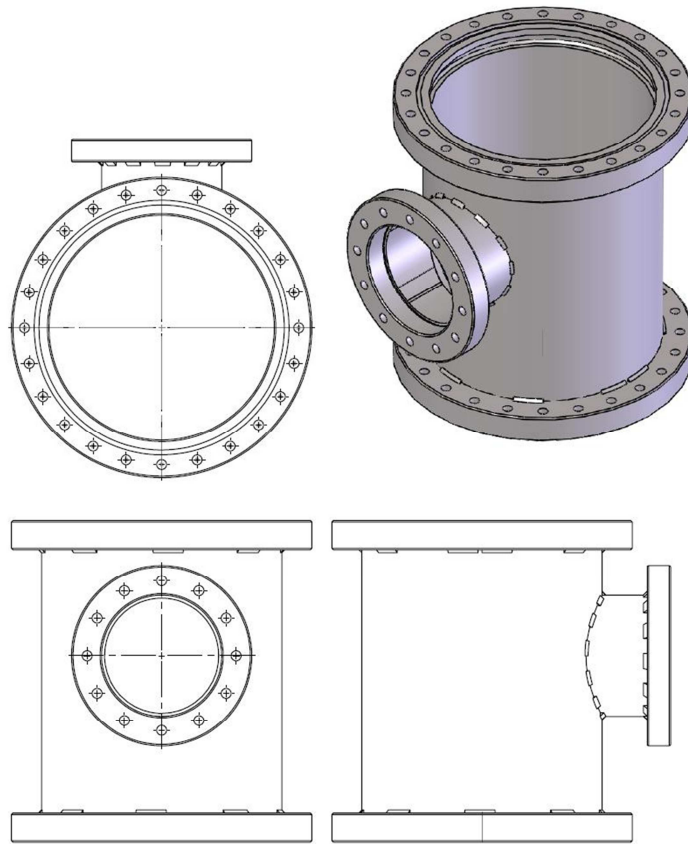


**Figure 2.2. Detailed drawing of the lower chamber section.**

Inside the lower chamber, the 4-PB tools, the load cell, and two thermocouples are installed. Figure 2.3 shows a closer view of the components that make up the 4-PB mechanism. First, an aluminum base is fastened to welded studs in the chamber and acts as an anchor. The load cell is attached to the anchor using two bolts and an M6X1 threaded rod. An aluminum block with channels on the top is fastened to the top end of the load cell using the same threaded rod. This block has 5 sets of channels machined into its top surface which are meant to hold dowel pins (5 mm in diameter for this research) in place. These pins provide to points of load application to the sample, and the distance between them be adjusted by selecting appropriate grooves in which to place the dowel pins. The last 2 loading points on the sample are facilitated by a loading block with fixed dimensions. Several loading blocks with different dimensions were machined from aluminum to facilitate samples of different sizes. The loading block is decoupled from the linear actuator and a ball bearing is placed between them. This configuration helps to eliminate loading misalignment if the sample becomes slightly tilted as a result of uneven crack propagation. One of the aforementioned thermocouples is placed at the base of the load cell, and the other is located below the pin holder. By comparing the difference in temperature between these two thermocouples, it is possible to discern if a temperature plateau is approaching. If a large difference in thermocouple readings exists, it is an indication that temperature is changing. In order to maintain consistent sample placement in the 4-PB rig, a datum tool is used. Figure 2.4 shows the datum tool as it fits with the pin holder. With the samples aligned directly in the middle of the datum tool, positioning repeatability can be achieved.

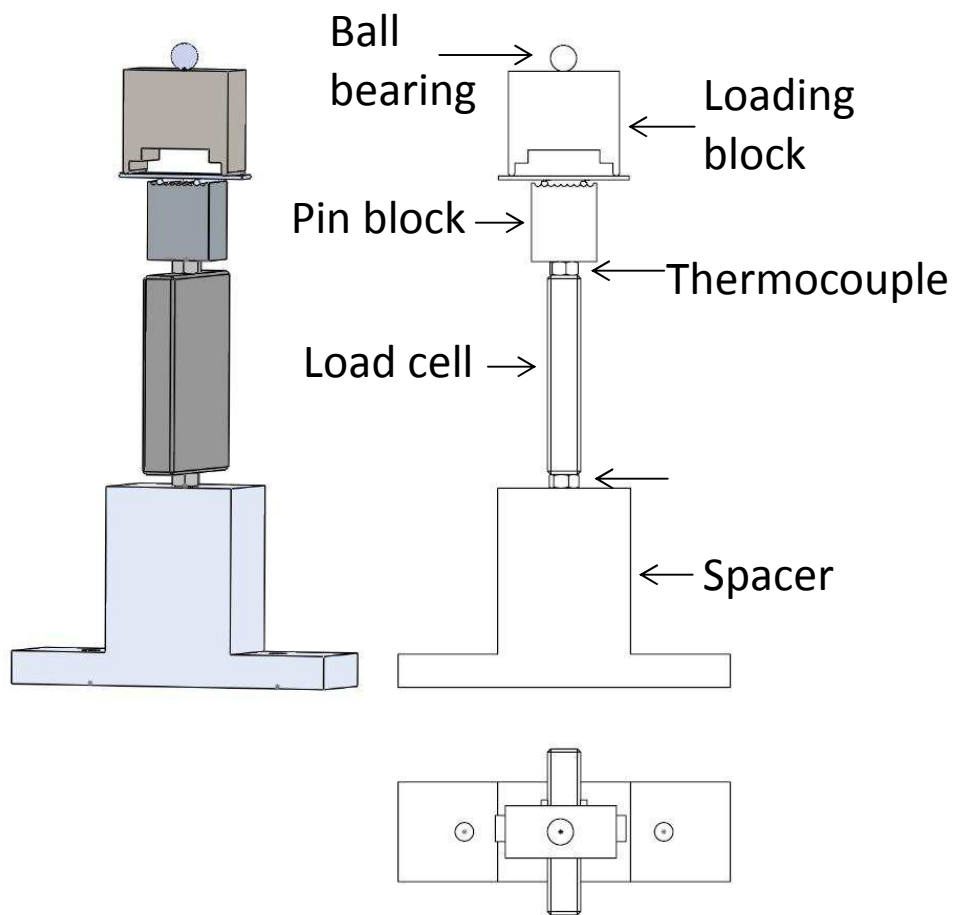


**Figure 2.3. Four-point bend components inside the chamber.**

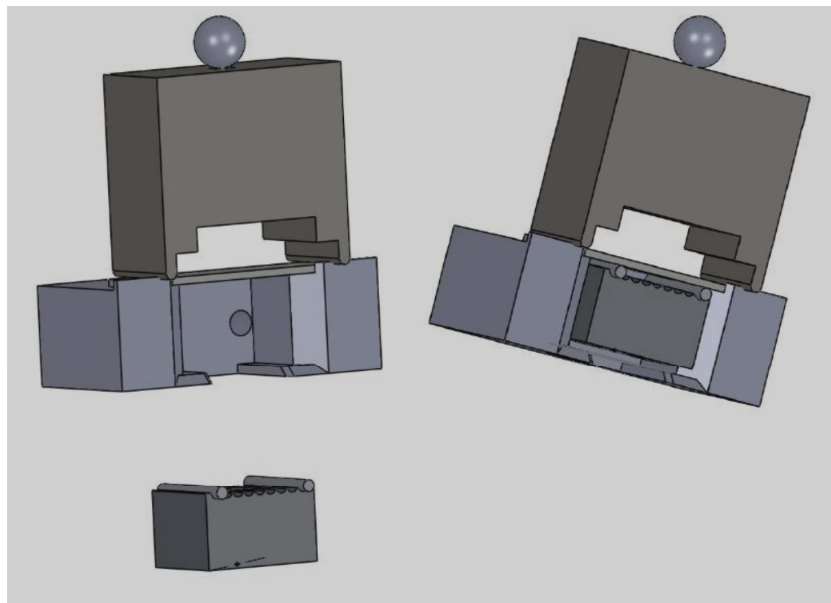


**Figure 2.4. The datum tool with a sample and the loading block (Left) and the datum tool positioning the sample and loading block on top of the pins (Right).**

### **2.2.2 MOTOR MOUNT**

Shown in Figure 2.5, the motor mount plate is constructed from a 10” double-sided ConFlat flange. The linear actuator is mounted to this component along with a thermocouple. This thermocouple is used to monitor the rate of temperature change of the motor which should be limited to 1 °C per minute according to the manufacturer. Eight through-holes of 1” diameter allow the flow of air and electrical conductors between the two sections of the instrument. An additional 1” diameter hole is placed directly beneath a viewport located in the top of the chamber in order to provide line of sight into the sample area for future optical positioning devices.

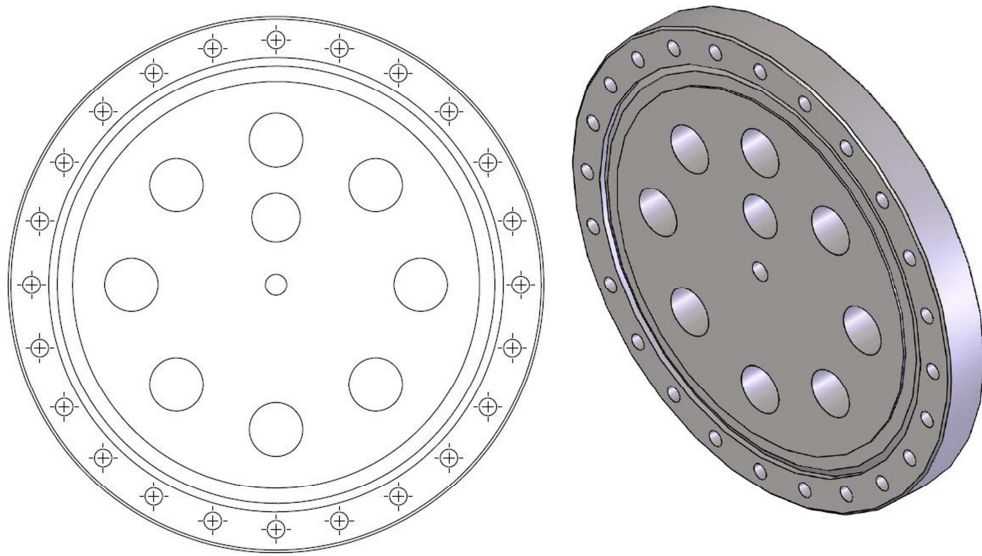


**Figure 2.5. Detailed drawing of the motor mount plate.**

### **2.2.3 UPPER CHAMBER**

The top section of the vacuum chamber is similar to the bottom section and is shown in Figure 2.6. The main purpose of this compartment is to enclose the linear actuator and provide ports for vacuum pump attachment. Two 6" ConFlat flanges are welded onto 4" pipes on the sides of this section. One port is used as a connection to the dual stage vacuum system, and the other is an access for service. It is possible to use this port to connect a third stage to the vacuum system. An ion pump is currently available for this purpose; however, it has not been used in this research.

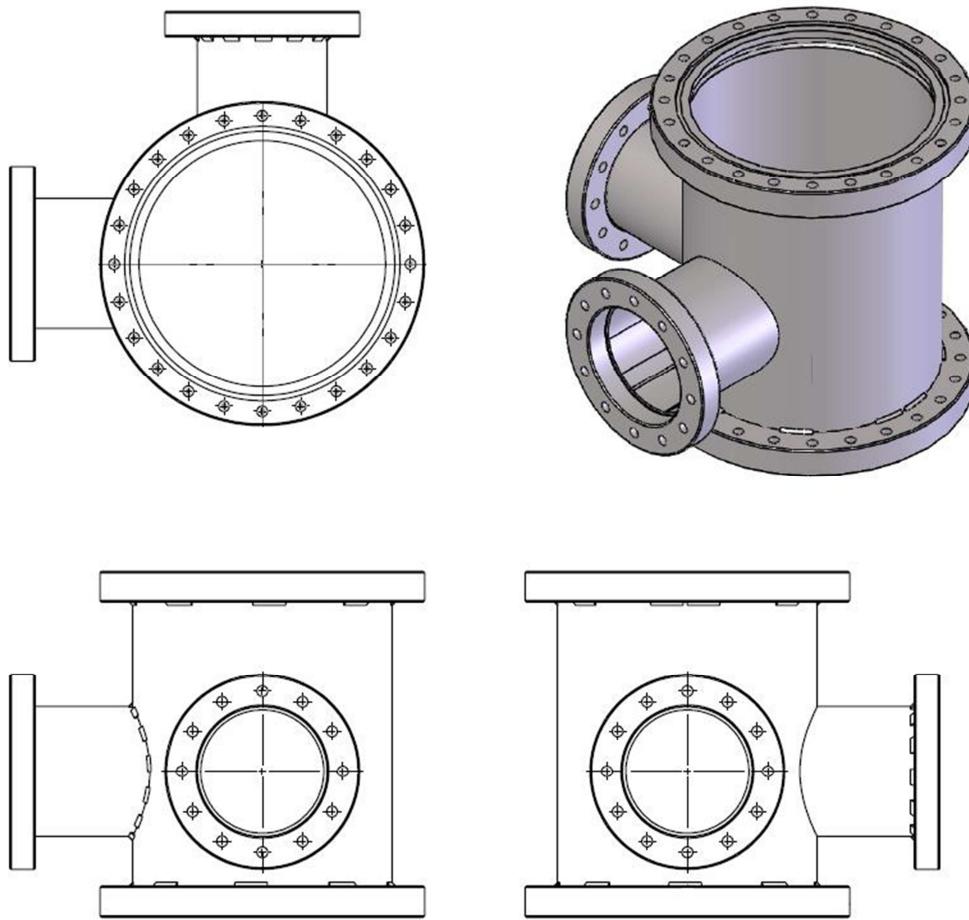


**Figure 2.6. Detailed drawing of the top chamber section.**

#### 2.2.4 FEEDTHROUGH PANEL

The feedthrough panel, shown in Figure 2.7, is equipped with four 1.33” and four 2.75” ConFlat flanges to which feedthroughs can be attached. Table 2.3 lists the purposes of each feedthrough on this panel. Each of flanges is mounted approximately 6” above the surface of the plate. This distance separates the temperature sensitive electronics from the rest of the chamber and creates a warming zone during low temperature tests. Furthermore, the small size of the tubes connecting the flanges to the chamber reduces the amount of energy and time required to achieve a temperature gradient according to Equation (22).

**Table 2.3. List of feedthroughs.**

Number	Type	Feedthrough
1	1.33”	2 X E-Type Thermocouple
2	1.33”	E-Type Thermocouple
3	1.33”	Load-Cell
4	1.33”	Unused
5	2.75”	Linear Actuator
6	2.75”	Pirani Cold Cathode Gauge
7	2.75”	Viewport
8	2.75”	Unused

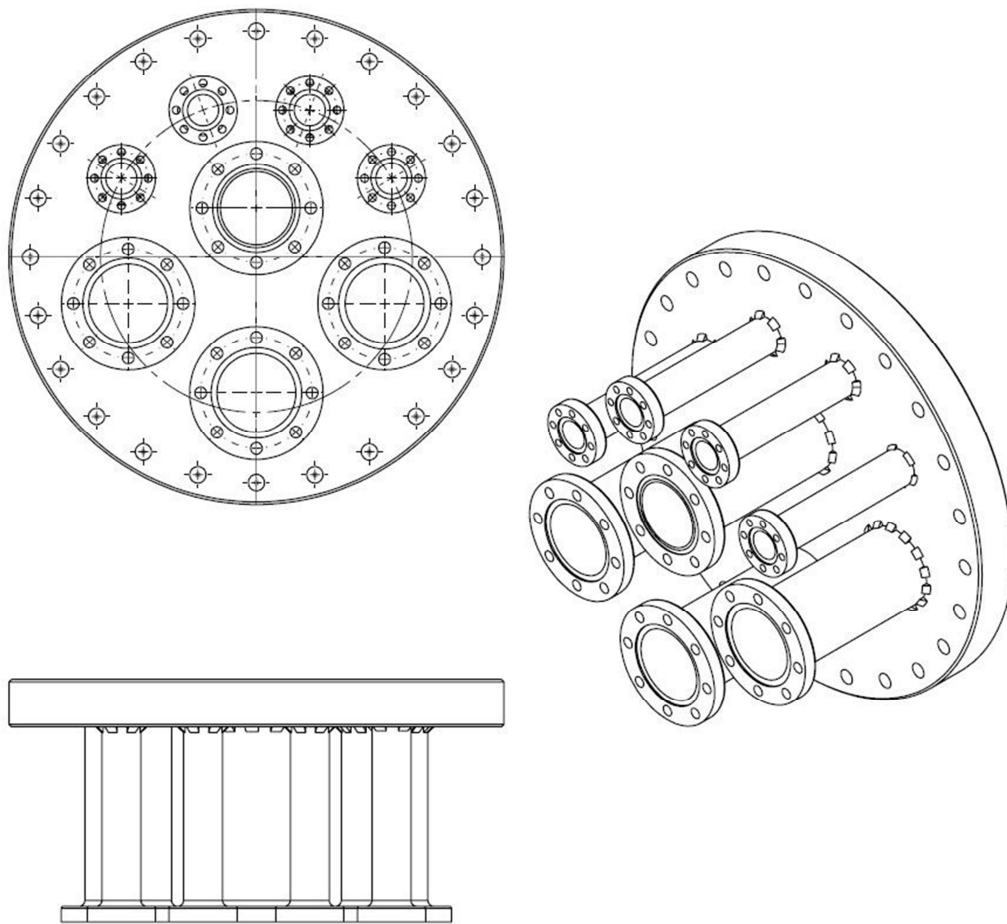


**Figure 2.7. Detailed drawing of the feedthrough panel.**

## 2.3 CHAMBER COMPLIANCE

The role of the environmental chamber is twofold: to act as a vacuum vessel, and to provide structural support for the load-displacement measurements. The compliance of the frame is observable in test results as an error in the displacement reading according to the following equation:

$$displacement = d_m - \frac{Load}{k_c} \quad (23).$$

In Equation (22),  $d_m$  is the displacement output from the motor and  $k_c$  is the chamber compliance. With only the displacement reading from the motor, it is necessary to determine the stiffness of the frame in order to calculate the true displacement applied to a sample.  $k_c$  is the sum of the stiffness of each individual part involved and the stiffness of each of the joints between them. In this case, contact between any two vacuum components occurs through welded flanges which are fastened together with 24 bolts. Each bolt is preloaded to 75% of proof strength. The force required to separate the joint is much greater than the force capacity of the load cell (50N); therefore, the joint compliance is ignored. To obtain  $k_c$ , the simulation function of SolidWorks 2010 is employed. This software allows for entire assemblies to be evaluated based on interactions between the separate parts in contact; however, ignoring the joint compliances, each part can be simulated separately. Figure 2.8 shows the distribution of the strain in the motor mount plate when a reaction load of 20 N is applied in the point of attachment of the linear actuator. The point of interest is the center of the flange, where the linear actuator is attached. Using this software package, the position of the through holes was optimized to reduce flexion during loading. Figure 2.9 shows the strain characteristics of the bottom vessel as a result of the 20 N reaction force transmitted from the motor mount. This part is fixed at the bottom and

the load is applied to the top flange where the motor mount is bolted. The presence of the viewport causes the strain to be uneven at the top rim and may result in a slight deviation of the linear actuator's travel from its vertical axis. By summing the displacements in these two parts, it is possible to determine how much deflection there is per 1 N of applied load. This deflection can be used in Equation (23) to calculate the true displacement at any time during an experiment. According to Figure 2.10, the strain in the frame of the test mechanism will amount to ~17 nm at the rated load of 50 N. For a typical 4-PB test, the displacement rate is ~250 nm per second [31] and total movement of 0.2 mm is needed. The compliance of the frame is less than 0.001% of the expected travel range; therefore, it can be neglected and a calculation of true displacement as described by Equation (23) is not necessary.

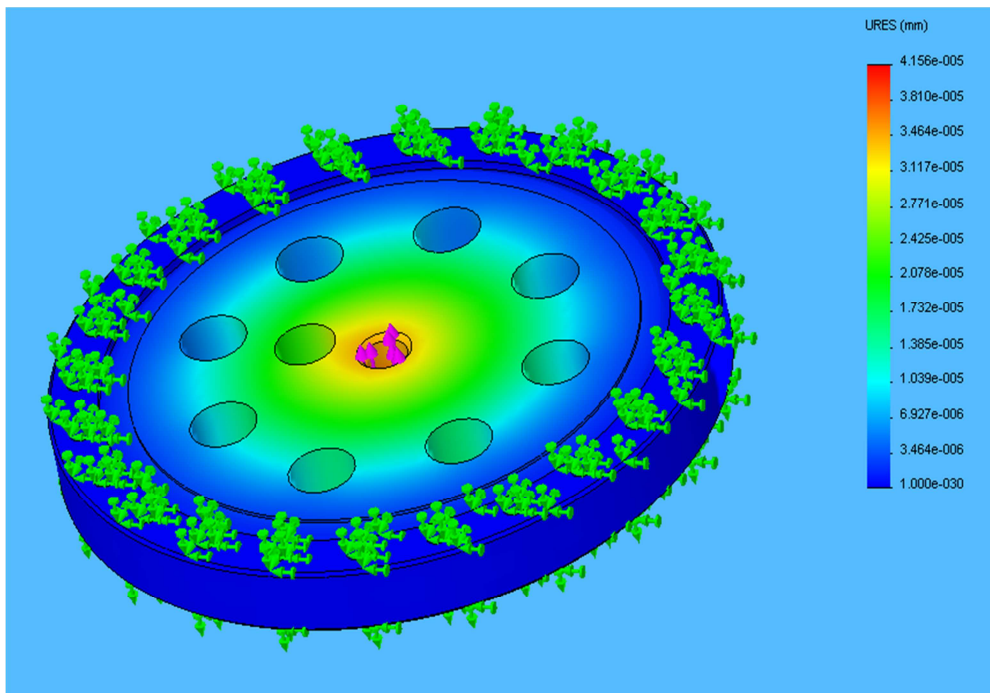


**Figure 2.8. Strain in the motor mount plate as a result of a 20N reaction force applied to the mounting location of the linear actuator.**

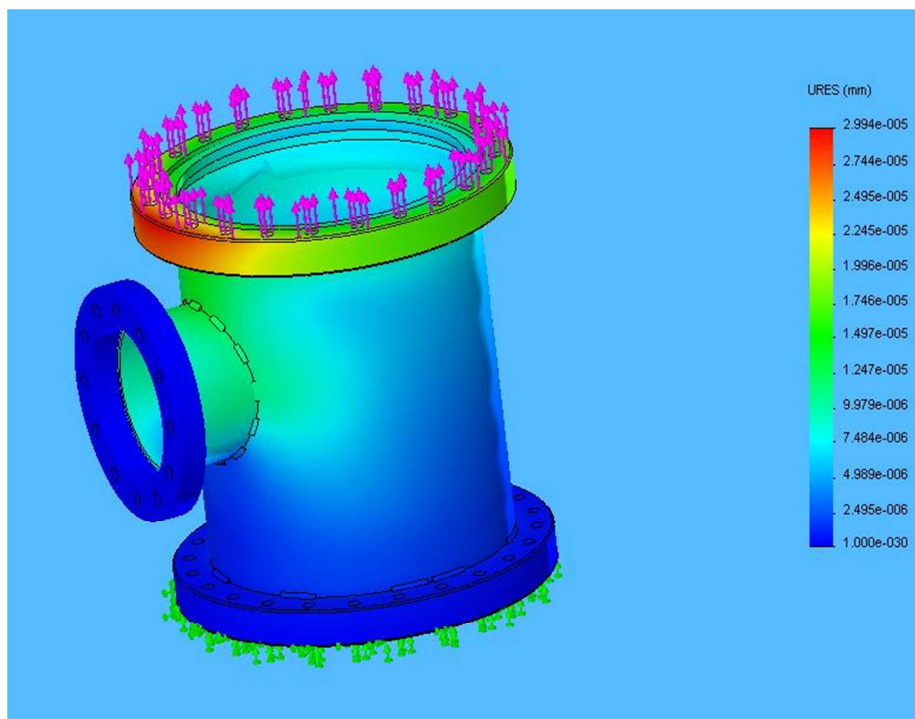


**Figure 2.9. Strain in the lower chamber as a result of a 20N reaction force applied to the mounting location of the motor mount plate.**

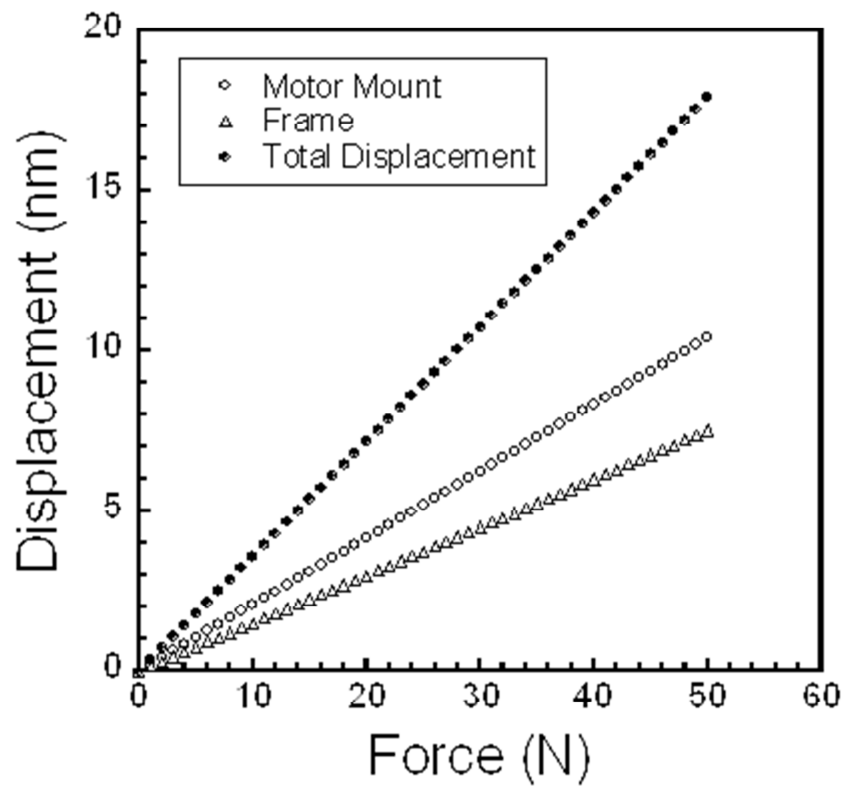


**Figure 2.10. Strain of the test instrument from zero to maximum loading.**

## 2.4 CALIBRATION AND STABILITY TESTING

The thin film mechanical tester described in this work is comprised of individual components that are capable of operating in the harsh environments outlined in the design requirements section. Prior to conducting tests in various conditions, it is necessary to assess the accuracy and performance of the machine components. The output of the load cell, for example, is affected by temperature variation. As temperature decreases, output voltage decreases by 0.0502% of full scale per degree Celsius. Initially, the repeatability and stability of the load cell is evaluated by placing a series of weights on it and recording the output over time. In Figure 2.11, it is evident that over a 4 hour time frame, the reading of the load cell does not show any upward or downward trend. Small fluctuations over time are evident and are attributed to electrical noise along with small variations in ambient temperature. In order to observe the impacts of -30 °C temperature on load cell output, simple 4-PB tests are conducted using a 1 mm thick and 25 mm wide glass slide (Fisherfinest<sup>®</sup> microscope slides). Figure 2.12 shows the load-displacement data generated at a chamber pressure of 0.46 Pa with one test at 20 °C and another at -30 °C. Since the load and displacement results measured at these two extreme conditions overlap, it is concluded that the instrument can produce consistent and reproducible results under different environments. According to the manufacturer of the load cell, the output of the load cell decreases by 0.0502% of full scale value per degree drop in temperature. This means a reduction of 1.26N is expected with a 50 °C temperature drop at full load. All values presented in this report are raw results as obtained from the load cell. This is because the specifications from the manufacturer may be worst case scenarios, and according to Figure 10, there is no discernable difference between the load-displacement ramps obtained at 20 °C and -30 °C.

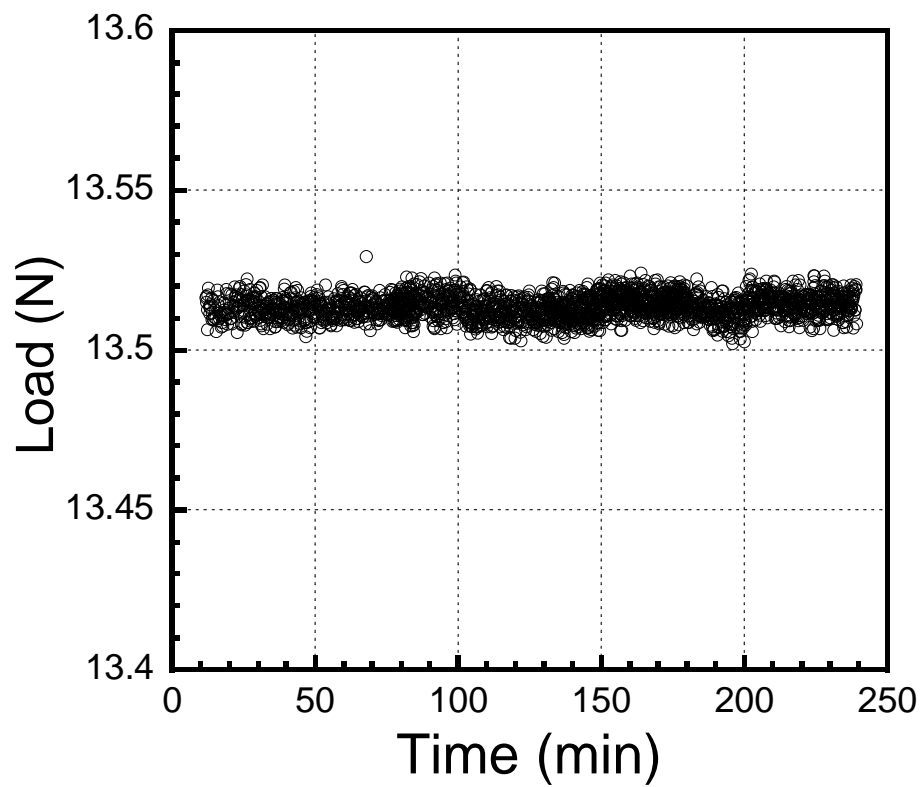


**Figure 2.11. Stability of the load cell under static loading conditions for ~4 hours.**

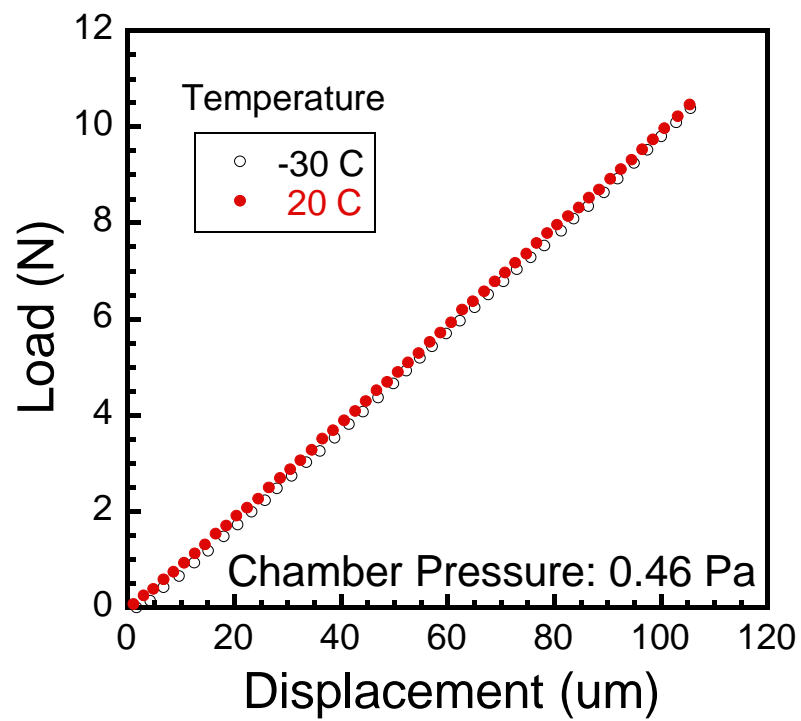


**Figure 2.12. Load-displacement curve of a glass slide measured at -30 °C and 20 °C.**

**The linearity and slope of the reading has not been impacted by the change in temperature.**

The temperature stability of the test instrument was evaluated by surrounding the lower chamber with dry ice and allowing the temperature to decline for approximately 4 hours until a plateau was reached at  $-50\text{ }^{\circ}\text{C}$ . At this point, additional dry ice was added to the chamber surroundings, and the temperature was recorded. Figure 2.13 shows that in this manner, the temperature of the test environment was kept constant for over 60 minutes with only  $1\text{ }^{\circ}\text{C}$  variation.

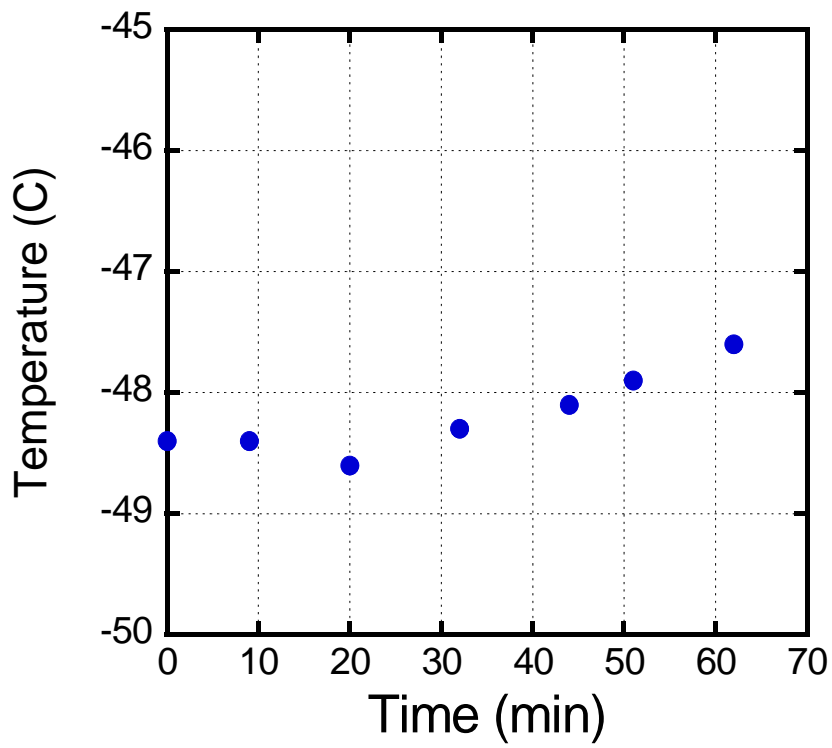


**Figure 2.13. Temperature stability of the environment chamber is shown over a 60 minute time frame during which a total fluctuation of 1 °C occurs.**

## CHAPTER 3 EXPERIMENT METHODS

In this chapter, the experiment methods used in this work are described. The four-point bend technique is discussed in detail and the specific parameters used in this research are outlined. The specific sample fabrication procedure is also described and the use of the epoxy bonding method for low temperature testing is validated by DMA testing as well as finite element analysis. Finally, the use of X-ray Photoelectron Microscopy to identify the fracture surface composition is introduced.

### 3.1 FOUR-POINT BEND TECHNIQUE

In this research, both the cohesive and adhesive fracture strengths of the thin film dielectrics were characterized by four-point bending (4-PB). This method was pioneered by Charalambides et al. [48-49] for measuring the mixed mode fracture resistance of biomaterial interfaces. They presented two methods for obtaining the stress intensity factors by numerical methods: the first being J-integral calculation and the second being crack surface displacement [48]. Their work showed that the J-intergral method is less reliant on mesh refinement. Furthermore, they characterized the impacts of friction and loading configuration on the energy release rate [49]. The 4-PB method was refined by Ma et al. [50-51], Dauskardt et al. [52], and Gage et al. [53] to accommodate thin film stacks. Typically, this method requires the film of interest to be sandwiched between two substrates, which is silicon in this research. First, a pre-crack is cut into one of the substrates to a depth of approximately half of the substrate's thickness. The sample is then loaded in 4-PB configuration as shown in Figure 3.1, and the vertical distance between the pins is reduced. The advancing rate for experiments in this research

is 250 nm per second. When force is applied to the sample, it enters a linear loading region which is shown in Figure 3.2. As the load increases, the pre-crack propagates down through the substrate until it reaches the film stack. This event results in a sharp drop in load. After reaching the film stack, the crack kinks and follows a stack component or interface in a horizontal direction. When the crack front becomes distant enough from the vertical pre-crack, ( $a > 2h$ ) [51], stress intensity becomes constant; therefore, the crack propagation rate reaches a steady state and a plateau is observed. The value of load at this plateau allows the steady-state energy release rate  $G_{SS}$  to be obtained analytically according to the following equation:

$$G = \frac{21(1-\nu^2)P^2l^2}{16Eb^2h^3} \quad (24).$$

In Equation (24),  $l$  is the moment arm that is created between each set of inner and outer pins,  $P$  is the total force exerted onto the beam,  $b$  is the width of the beam,  $h$  is the wafer's thickness, and  $E$  and  $\nu$  are the elastic modulus and Poisson's ratio of the bulk substrate. The velocity of the crack can be obtained using the following relation:

$$v = \frac{8Eb^3}{21(1-\nu^2)l^2P} \left( \frac{dD}{dt} \right) \quad (25).$$

In Equation (25),  $dD/dt$  is the vertical displacement rate imposed on the sample. Hughey et al. [54] showed that fracture energy is greater when larger displacement rates are used; therefore, the displacement rate used in the experiments in this work is kept constant at 0.25  $\mu\text{m/s}$ . Two separate thin film fracture instruments are used in the current study. One offers control of the pressure and temperature while the other is robust and allows samples to be submerged in liquid. The Spacing between the inner and outer pins  $l$  is 15.6 mm on the environmental machine and 13.9 mm on the other.

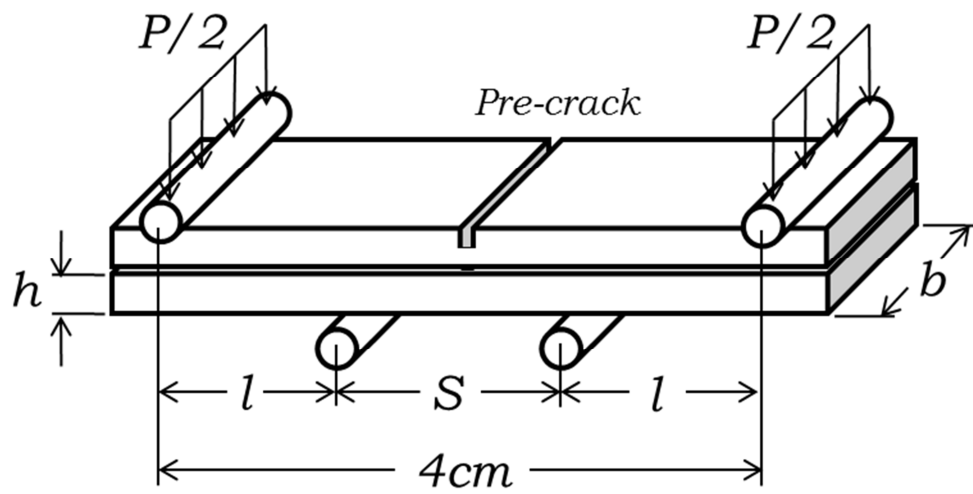


**Figure 3.1. Thin film fracture specimen in four-point bend configuration.**

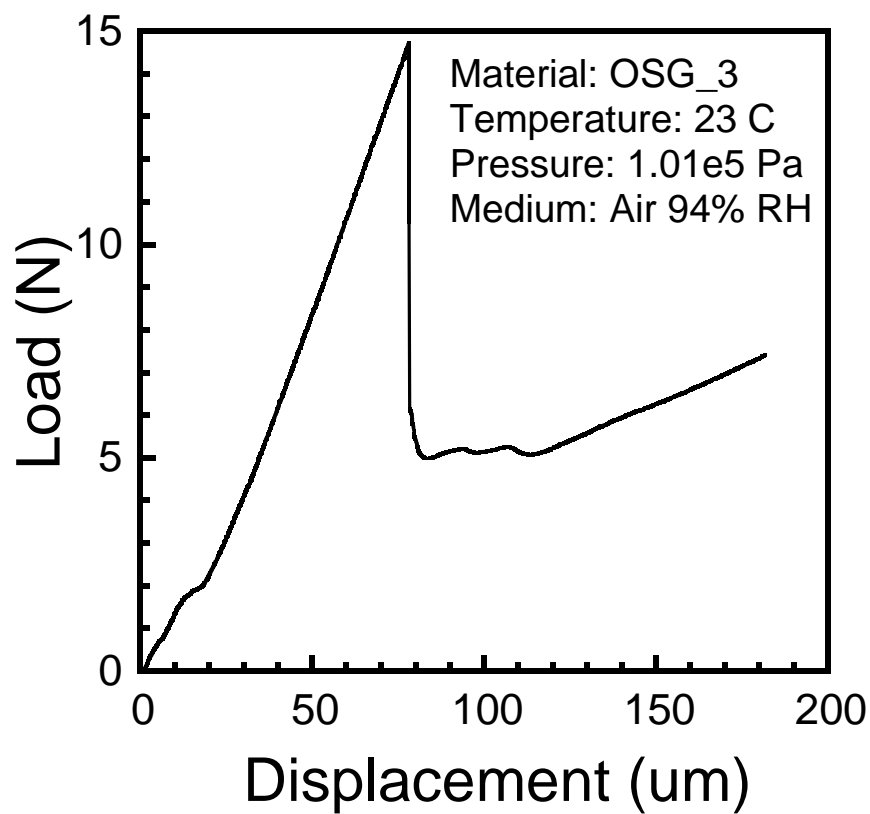


**Figure 3.2. Load-displacement curve of a typical OSG/SiCN film stack. Initially, elastic deformation occurs. The sharp drop in load (near 80  $\mu\text{m}$  displacement) corresponds to pre-crack propagation to the surface of interest.**

### 3.2 SAMPLE FABRICATION

The sample preparation process began with deposition of OSG films onto 300 mm (1-0-0) silicon by plasma-enhanced chemical vapor deposition (PECVD). The precursor used was diethoxymethylsilane (DEMS) while helium and oxygen served as carrier and oxidizer gases respectively. Depositions were performed at 250 °C using appropriate ratios of a proprietary aromatic porogen to construct the sacrificial porogen phase. These organic molecules were then removed by irradiation at 400 °C using broadband UV radiation in vacuum. Three different types of OSG thin films, OSG\_1, OSG\_2, and OSG\_3, were deposited with porosity values of ~ 20.1%, 27.2%, and 44.5%, respectively. These films have the corresponding dielectric values of ~ 2.60, 2.43, and 2.30. The relative dielectric constants of the films were measured using a Quantox XP metrology system (KLA-Tencor Corp., Milpitas, CA). Subsequently, all of the OSG films were capped with ~300 nm thick PECVD silicon carbonitride (SiCN) thin film which has a dielectric constant of approximately 5.0. The prepared wafers were first cleaved into ~5 cm by ~1 cm strips by hand. They were then bonded together with the film stacks adjacent to each other using epoxy adhesive (Epotek 353ND). The film stack is shown in Figure 3.3. To cure the adhesive, these samples were baked in a convection oven at ~45 °C for 20 minutes and then at ~85 °C for an additional 40 minutes. The pre-notch was created by hand using a 4" diamond dicing saw (Buehler - Isomet Low Speed) to a depth of approximately half of the wafer thickness (350 μm). Experiment results show that the depth of the pre-notch does not affect the fracturing characteristics as long as cracks from the dicing blade do not penetrate the film stack; therefore, very low speed and applied pressure was used (60 RPM) for this procedure. All samples were stored under flowing nitrogen gas conditions and baked at 85 °C for 20 minutes immediately prior to testing in order to remove moisture.

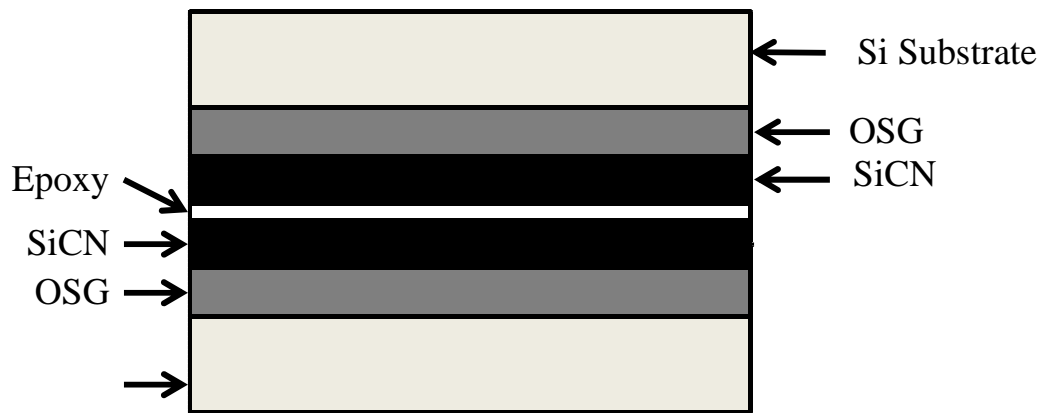


**Figure 3.3. Film Stack Diagram (Not to scale).**

### 3.3 THERMAL-MECHANICAL PROPERTIES OF EPOTEK 353ND EPOXY

To confirm the thermal-mechanical stability of the epoxy adhesive, the load-displacement response of an epoxy beam (7.9 mm width and 2.3 mm thickness) under four-point bend loading at temperatures of 23°C, 0°C, -20°C, and -40°C are plotted in Figure 3.4. The displacement rate used in this experiment was 1  $\mu\text{m/s}$ . This figure shows that the elastic deformation behavior of this material is not noticeably different within the temperature and pressure range of our experiments. In Figure 3.5, results of a dynamic mechanical analysis (DMA) test performed in accordance with ASTM E1640 are shown. This is a standard test method for assignment of glass transition temperature to the epoxy [55]. Compared to the storage modulus at room temperature (2.59 GPa), a change of 16% occurs as temperature drops to -40 °C. Figures 3.4 and 3.5 show only slight changes in release modulus within the range of conditions of this work, and indicate that EPOTEK 353ND is a suitable material to be used for 4-PB experiments.

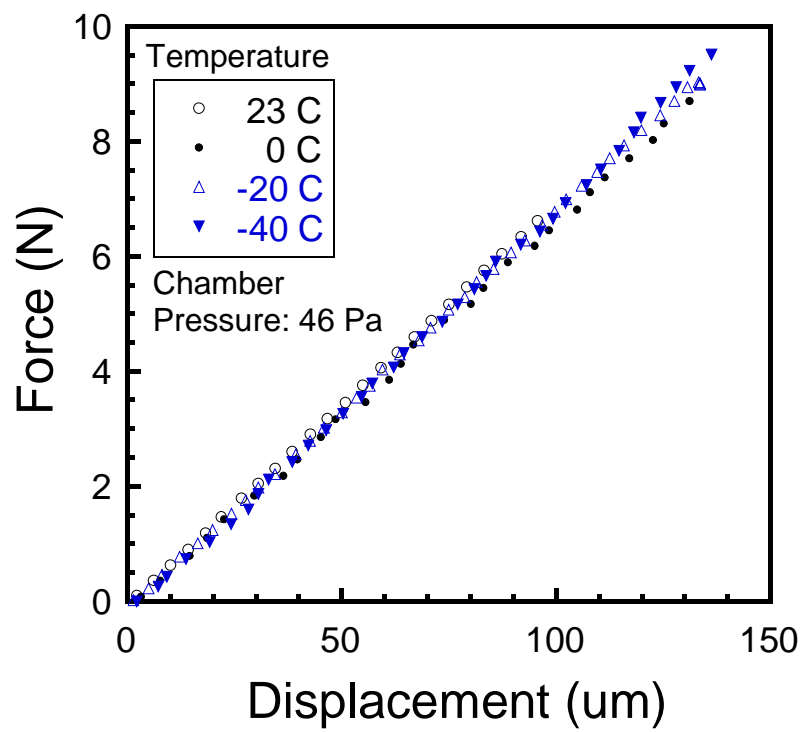
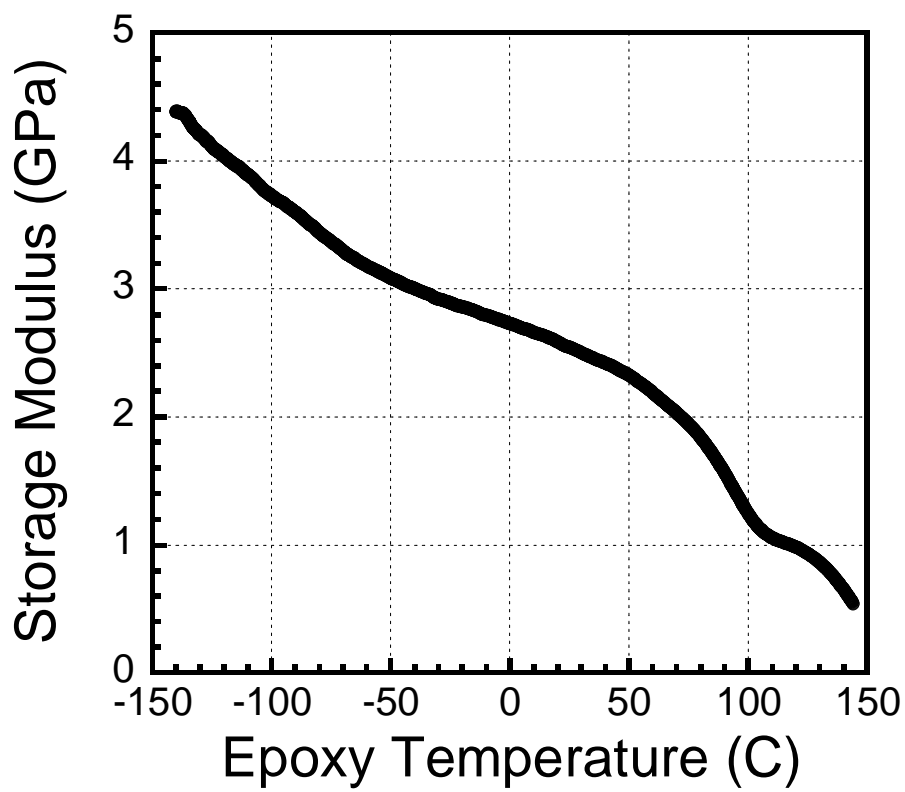


Figure 3.4. Load-displacement curves of an epoxy beam at 23 °C, 0 °C, -20 °C, and -40 °C.



**Figure 3.5. DMA results showing the change in the storage modulus of EPOTEK 353ND epoxy.**

### 3.4 FINITE ELEMENT METHODS

A fully elastic 2-D finite element model of the four-point bend sample was constructed using ABAQUS CAE software package. The intent of this model was to investigate the effect on the stress intensity factors at the crack tip of a four-point bend sample when an epoxy layer with a storage modulus of 3 GPa is added. Figure 3.6 shows the geometry of the model that was created. By using an x axis symmetric constraint at the midpoint, it is possible to model only one half of a sample. The load and y axis constraints are applied according to the true sample geometry and scale. An accurate scale was also used for the relative size of each component in the film stack as well as the substrates. Since steady-state fracture is expected when the crack is sufficiently long to satisfy the following expression:

$$a > 2h \quad (26).$$

In Equation (26),  $a$  is the crack length and  $h$  is the thickness of the substrate [51]. In order to meet this requirement, a 4 mm long crack (seam) was constructed within the OSG layer. A seam prevents the software from automatically joining the nodes of the adjacent elements along the crack front and allows the layers to separate during loading. Figure 3.7 shows sections of the mesh as well as the overall appearance of the model before and after load application. A structured mesh using predominantly 8-node quadrilateral elements was created with progressive refinement based on proximity to the crack tip. The elements around the crack tip were collapsed down to triangles such that three nodes occupy the same point in space. Since this is an elastic model, the mid-side nodes of these triangular elements were moved to the  $\frac{1}{4}$  points to create the  $\frac{1}{\sqrt{r}}$  strain singularity and enhance numerical accuracy. Using a “spider web” meshing technique, a smooth transition from the fine mesh at the crack tip to a coarse mesh in the distal region was

established. This technique also provided concentric rings of quadrilateral elements along which integration contours for J-integrals were evaluated. Overall, the model was comprised of 72,248 nodes which created 71,581 linear quadrilateral and 70 linear triangular elements. The J-integrals along three contours around the crack tip were calculated to evaluate the refinement of the mesh. The result of this study is presented in Figure 3.8 and shows adequate convergence since the three curves are nearly overlapping. The J- integrals over the two outer curves are overlaid on top of each other while the integral of the inner-most curve differs by ~15% at the last time-step.

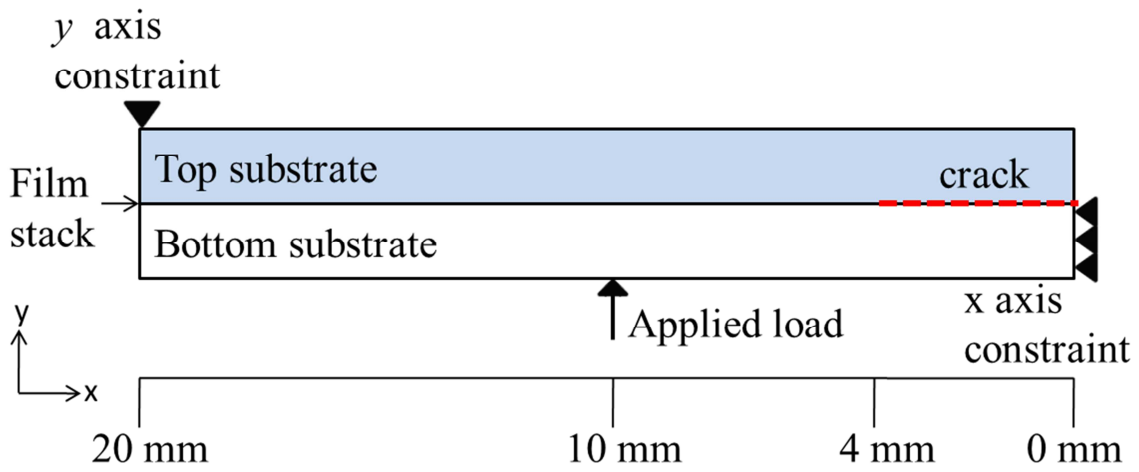


**Figure 3.6. Geometry of the finite element model.**

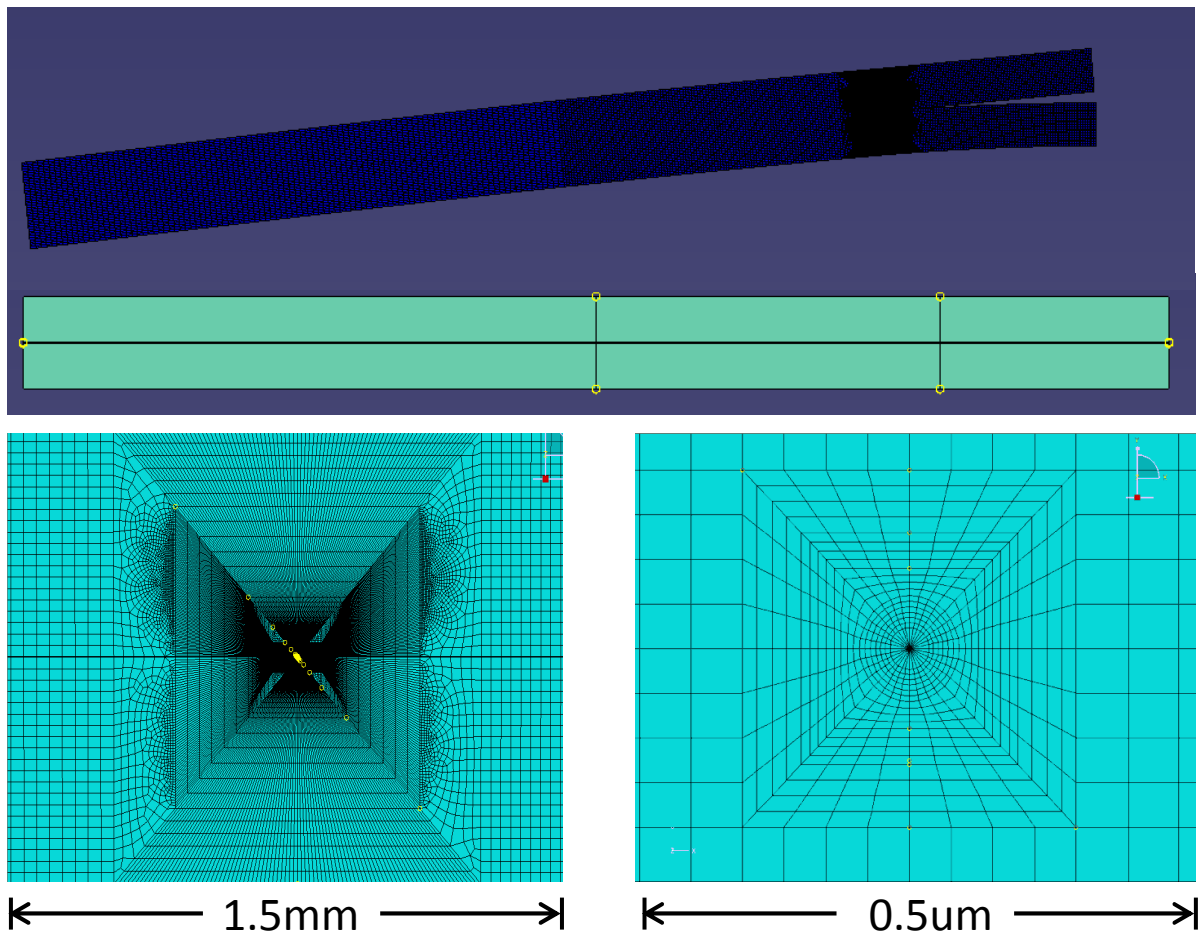


**Figure 3.7. Finite element model of the four-point bend sample shown before and after deformation (top), close-ups of the mesh structure (bottom).**

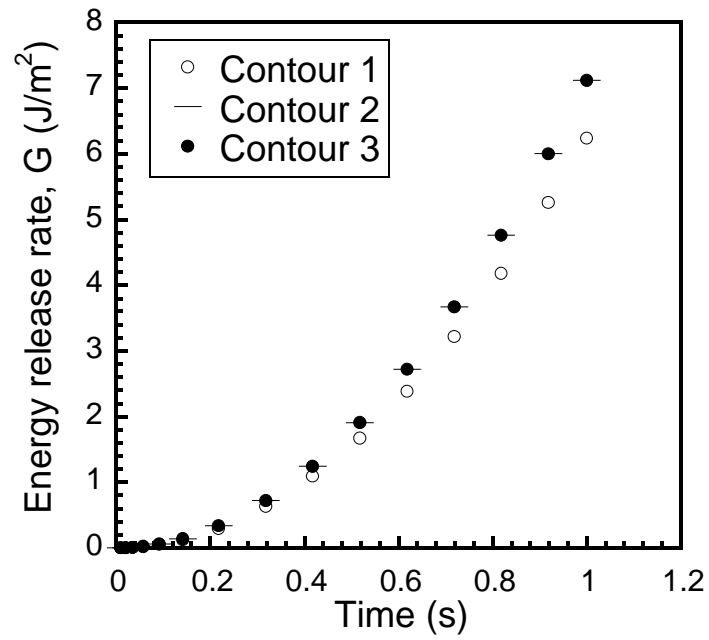


**Figure 3.8. J-integral convergence study.**

This model was used to simulate the effect of the epoxy layer on the fracture phase angle which was defined previously by Equation (16). Two studies were conducted using storage moduli of 3GPa and 100MPa for the epoxy. Figure 3.9 shows that changing the epoxy layer thicknesses from 0  $\mu\text{m}$  to 2.0  $\mu\text{m}$  results in a decrease in the phase angle from  $\sim 40.5^\circ$  to  $\sim 25.7^\circ$  when the modulus is 3GPa, and from  $\sim 40.5^\circ$  to  $\sim 10.4^\circ$  when the modulus is 100MPa. This means that in a perfectly elastic case, mode I fracture dominates as the epoxy thickness increases and less energy is expended on contact friction, blunting, and plasticity [56]. This means that a smaller amount of energy is required to drive the fracture, demonstrating that the addition of a compliant layer such as a polymeric low-k dielectric or an organic thin film to a system will have a detrimental impact on overall fracture resistance and reliability.

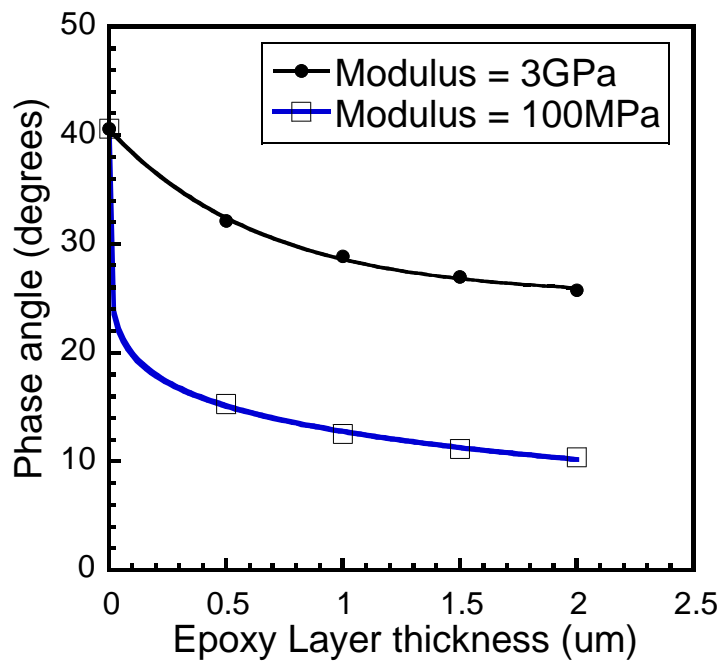


**Figure 3.9. Phase angle as a function of epoxy layer thickness for two different elastic moduli.**

### 3.5 CRACK INTERFACE IDENTIFICATION BY XPS

In order to identify the crack interface in the 4-PB samples, each sample must first be opened to reveal the 2 crack surfaces. This was accomplished by creating a score mark on the silicon wafer opposite to the one with the pre-crack, approximately 1 cm away from the center. Figure 3.10 shows the location of this score line which exposes 1 cm of fracture surface. All the XPS tests were performed using a Thermo Scientific K- $\alpha$  machine (Thermo Scientific Inc., West Palm Beach, FL). This device uses a monochromated Al K- $\alpha$  x-ray source with a variable spot size of 30-400  $\mu\text{m}$ . For reference when determining the location of the crack, the XPS spectra of SiCN and OSG\_1 are displayed in Figure 3.11. Also shown is a spectrum which looks to be similar to that of OSG\_1 but has slightly different relative peak values and an extra peak at  $\sim 400$  eV. The resemblance of this spectrum to that of OSG indicates that this is an interfacial fracture occurring at the boundary of OSG and SiCN. Since nitrogen is not found in the OSG layer, the presence of the small nitrogen peak may indicate that the crack is mainly in the OSG layer with periodic exposure of the SiCN.

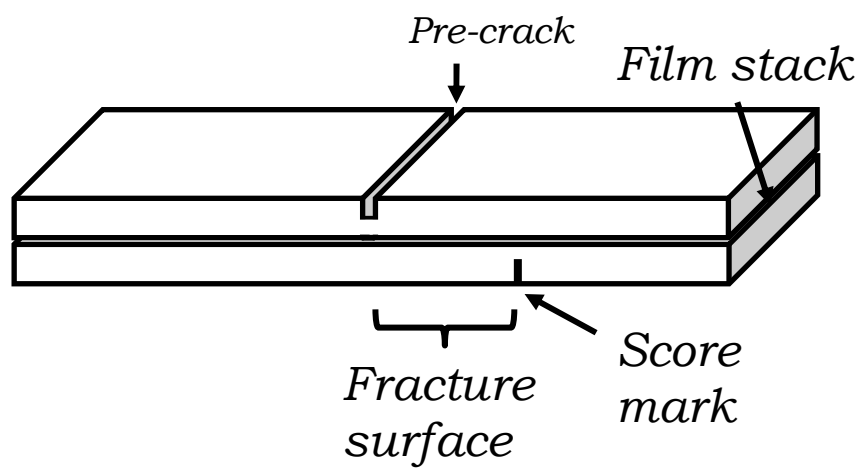


**Figure 3.10. Sample gently broken along score mark to reveal the fracture surfaces for subsequent XPS.**

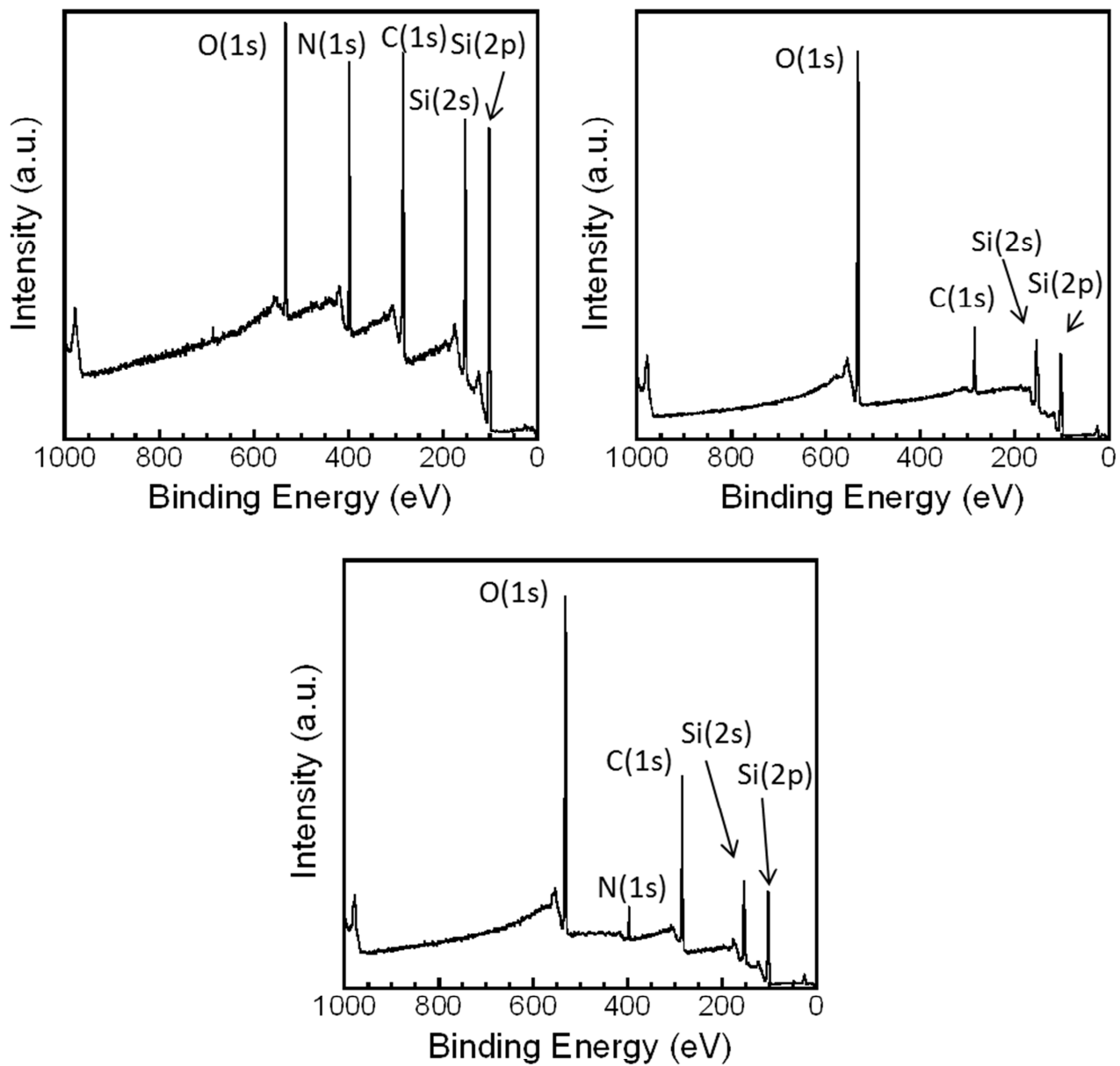


**Figure 3.11. Spectra of SiCN (top left), OSG\_1 (top right), interfacial surface OSG\_1/SiCN (bottom).**

## CHAPTER 4 RESULTS AND DISCUSSION

In this chapter, the results of the experiments on OSG\_1, OSG\_2, and OSG\_3 are presented. The conditions under which each film was tested are shown and the effects of humidity and low temperature on the fracture toughness of these materials are discussed in detail.

### 4.1 HUMIDITY EFFECTS ON OSG/SiCN THIN FILM FRACTURE STRENGTH

Room temperature fracture energy ( $G$ ) values of all three OSG/SiCN film stacks measured in various relative humidity (RH) conditions are shown in Figure 4.1. This figure also includes results from specimens tested in DI water and high purity nitrogen (Praxair NI4.8, 99.998%) environments. The water partial pressures of these two conditions are assumed to be 2612 Pa which is the saturated water vapor partial pressure at 22 °C, and 3.03E-3 Pa which is the maximum moisture concentration in the nitrogen supply (3 ppm) as specified by the supplier. A summary of the testing conditions and the fracture energy data from these experiments is listed in Table 4.1. Fracture tests performed in (DI) water and 70% RH were not carried out in the cryogenic load-displacement sensing instrument due to the moisture sensitivity of the electronics in this equipment. Instead, they were carried out in another thin film adhesion tester with the same load – displacement capabilities but with a higher tolerance for moisture in the environment. To calculate the crack propagation velocity ( $v$ ) of these experiments, Equation (25) was used. Velocity results are also listed in Table 4.1 and range from 22 to 41  $\mu\text{m/s}$ . Figure 4.1 shows that the fracture strengths of all thin film specimens in this work are sensitive to the amount of moisture in the environment. Less energy is required to create crack propagation when

the environment contains more water molecules. The results show that the fracture energy is the lowest when the sample is submerged in DI water and the G values converge to  $\sim 2.5 \text{ J/m}^2$  for all films. This indicates that the fracture strength of the OSG in this testing condition does not appear to depend on the film porosity. As the moisture content in the environment decreases, the fracture resistance of the OSG/SiCN samples increases exponentially; However, the fracture energy reaches a plateau value when the moisture concentration is near 6% RH. Thereafter, further reduction of moisture in the environment does not have a significant effect on improving the fracture strengths of the OSG/SiCN specimens. In contrast to the fracture energy measured when submerged in DI water, this plateau value appears to be influenced by the porosity of the OSG film. The average fracture energies for OSG\_1, OSG\_2, and OSG\_3 in a pure nitrogen environment have values of  $7.65 \pm 1.85 \text{ J/m}^2$ ,  $5.23 \pm 0.57 \text{ J/m}^2$ , and  $4.45 \pm 0.58 \text{ J/m}^2$  respectively, with the one standard deviation of data spread. These results are shown in Figure 4.2 and are consistent with the observations by Li et al. [9] and Guyer et al. [30] who demonstrated that OSG films are stronger when they contain a smaller amount of porosity. A linear fit of the OSG\_1/SiCN energy release rates in Figure 4.1 shows the moisture sensitivity coefficients (A and B) defined in Equation (21) have the values of  $2.02 \text{ J/m}^2$  and  $18.33 \text{ J/m}^2$ , respectively. The same constants for the OSG\_3/SiCN samples are  $0.84 \text{ J/m}^2$  and  $9.31 \text{ J/m}^2$ , respectively.

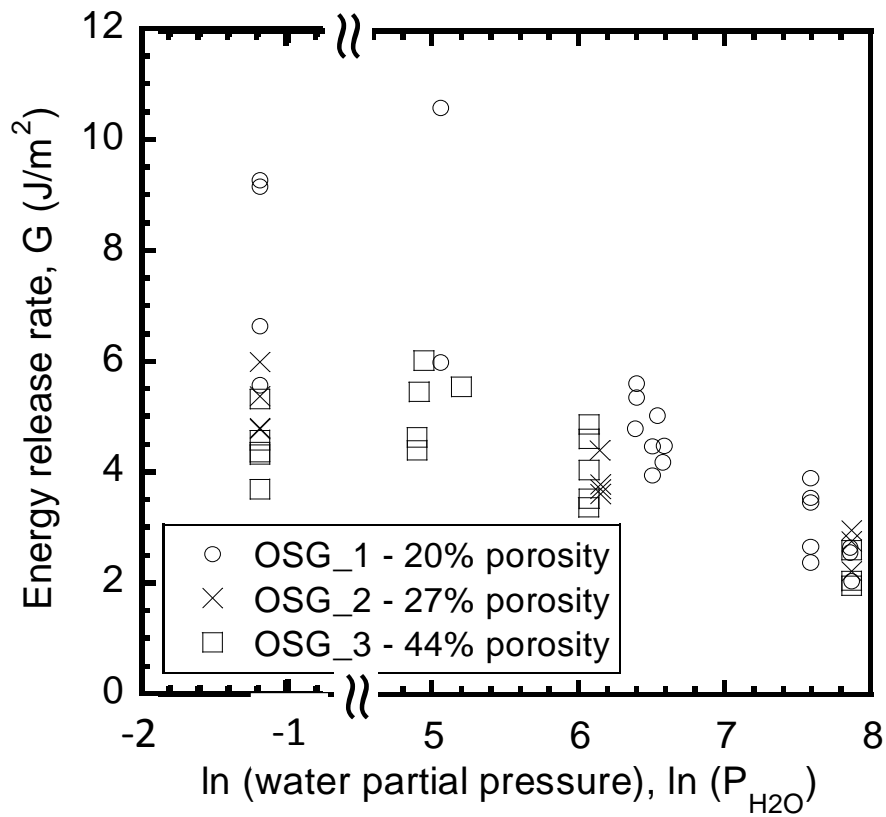


**Figure 4.1. Energy release rate of OSG/SiCN film stacks as a function of  $\ln(\text{water vapor partial pressure})$ . Also included are specimens tested in DI water and in a nitrogen environment.**

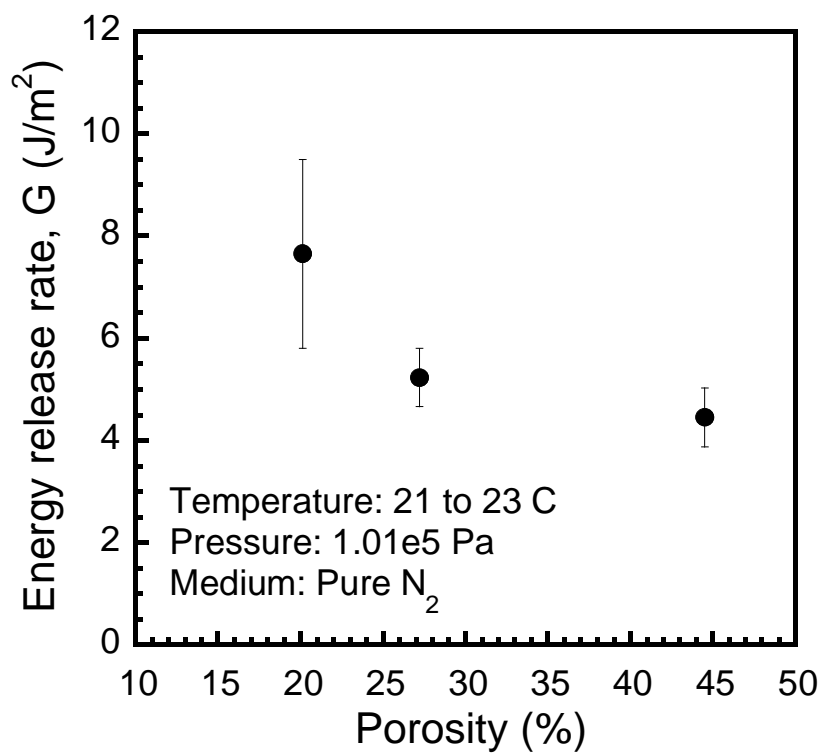


**Figure 4.2. Energy release rate of OSG films as a function of porosity (%) showing a downward trend with increasing porosity.**

**Table 4.1a. Testing conditions and results of OSG\_1/SiCN film stacks.**

Group	Temp (°C)	Pressure (Pa)	Purge medium	Avg. crack velocity (um/s)	Energy release rate (J/m <sup>2</sup> )	Avg. energy release rate (J/m <sup>2</sup> )	Std. dev.
OSG_1-1	22	101325	DI H <sub>2</sub> O	41.1	2.04, 2.66, 2.57	2.42	0.33
OSG_1-2	23	101325	air (70% RH)	36	3.47, 2.67, 3.56, 3.91, 2.38	3.20	0.64
OSG_1-3	22	101325	air (25% RH)	30.1	5.63, 4.81, 4.20, 5.37, 3.97, 4.49, 4.50, 5.05	4.75	0.57
OSG_1-4	22	101325	air (6% RH)	22.7	6.0, 10.62	8.31	3.3
OSG_1-5	23	101325	Pure N <sub>2</sub>	23.4	9.15, 9.27, 6.62, 5.57	7.65	1.85
OSG_1-6	22	1.60-04	Air (29% RH)	30.7	4.82, 3.83, 4.34	4.33	0.50

**Table 4.1b. Testing conditions and results of OSG\_2/SiCN film stacks.**

Group	Temp (°C)	Pressure (Pa)	Purge medium	Avg. crack velocity (um/s)	Energy release rate (J/m <sup>2</sup> )	Avg. energy release rate (J/m <sup>2</sup> )	Std. dev.
OSG_2-1	22	101325	DI H <sub>2</sub> O	44.1	2.76, 2.96, 2.23	2.65	0.38
OSG_2-2	21	101325	air (18% RH)	34.6	4.42, 3.71, 3.63, 2.66, 3.80	3.65	0.63
OSG_2-3	23	101325	Pure N <sub>2</sub>	27.9	5.98, 5.36, 4.79, 4.78,	5.23	0.57
OSG_2-4	23	4.00e-01	air (40% RH)	30.8	3.93, 4.06, 6.19, 3.61, 4.09	4.37	1.03
OSG_2-5	23	8.60	Pure N <sub>2</sub>	33.3	4.48, 3.05, 3.38, 3.91	3.71	0.63
OSG_2-6	21	1.60e-04	Air (22% RH)	29.4	3.90, 4.17, 4.50, 5.48	4.72	0.68
OSG_2-7	-30	4.60e-01	Air (22% RH)	31.3	4.74, 3.69, 3.76, 4.48	4.17	0.52

**Table 4.1c. Testing conditions and results of OSG\_3/SiCN film stacks.**

Group	Temp (°C)	Pressure (Pa)	Purge medium	Avg. crack velocity (um/s)	Energy release rate (J/m <sup>2</sup> )	Avg. energy release rate (J/m <sup>2</sup> )	Std. dev.
OSG_3-1	22	101325	DI H <sub>2</sub> O	48.4	2.61, 2.05, 1.97	2.21	0.35
OSG_3-2	23	101325	Ambient air (94% RH)	42.4	3.41, 3.85, 2.53, 3.56, 2.36, 2.07	2.96	0.73
OSG_3-3	21	101325	ambient air (17% RH)	31.6	3.38, 4.63, 4.89, 4.06, 3.54	4.10	0.66
OSG_3-4	25	101325	ambient air (5% RH)	27.9	5.57, 6.04, 4.65, 5.48, 4.42	5.23	0.68
OSG_3-5	22	101325	Pure N <sub>2</sub>	30.3	3.69, 4.36, 4.58, 5.31, 4.32	4.45	0.58
OSG_3-6	22	5.00e-01	ambient air (4% RH)	30.3	4.38, 4.94, 3.95	4.42	0.50
OSG_3-7	21	1.60e-04	ambient air (17% RH)	31.0	3.33, 4.15, 3.87, 4.54, 5.22, 4.54	4.28	0.65
OSG_3-8	-33	4.60e-01	ambient air (10% RH)	27.2	3.29, 5.18, 6.17, 5.55, 5.05, 5.56	5.50	0.44

To identify the locus of failure, fractured surfaces of these specimens were characterized by the X-ray photoelectron spectroscopy (XPS). The spectrums collected from the OSG\_1/SiCN samples fractured in DI water, 70% and 25% RH air, and pure nitrogen gas are shown in Figure 4.3 and the elemental compositions of these fractured surfaces are listed in Table 4.2. The results reveal that the fracture surfaces of 70% RH ambient air and pure nitrogen gas specimens contain oxygen, carbon, and silicon, and have a notable absence of nitrogen. This suggests that cracks did not propagate at the OSG\_1/SiCN or Si substrate/OSG\_1 interfaces. Instead, these fracture events were cohesive in nature with cracks extending within the OSG\_1 film. In contrast to the aforementioned, the DI water submerged sample, the XPS spectra show different elemental compositions between the two fracture surfaces with one contains nitrogen while the other does not. The surfaces that contain nitrogen correspond to the SiCN film while the other surface is the OSG layer which is nitrogen free. This indicates that when submerged under DI water, the adhesion energy of OSG\_1/SiCN is reduced and the crack propagates through the interface instead of the bulk material. One of the possible explanations for the change in failure sites from cohesive to adhesive is the fast moisture diffusion rate at the OSG\_1/SiCN interfaces as reported by Lin et al. [42]. They characterized the diffusion of water into the OSG/SiN<sub>x</sub> stacks using dynamic SIMS in depth profiling mode and a tracer isotope. Their results show water molecules tend to diffuse along the OSG/SiN<sub>x</sub> interface faster than through the bulk OSG film. The fast moisture diffusion rate at the interface increases the moisture concentration at the local crack tip and weakens the interfacial strength. Figures 4.4 and 4.5 show the XPS spectra of OSG\_2 and OSG\_3 fracture surfaces at various moisture concentrations and the chemical compositions of their fractured surfaces are listed in Table 4.2. The presence of nitrogen on one of the two

fracture surfaces indicates that cracks propagate along the OSG/SiCN interface for these two film stacks, i.e. adhesive failure.

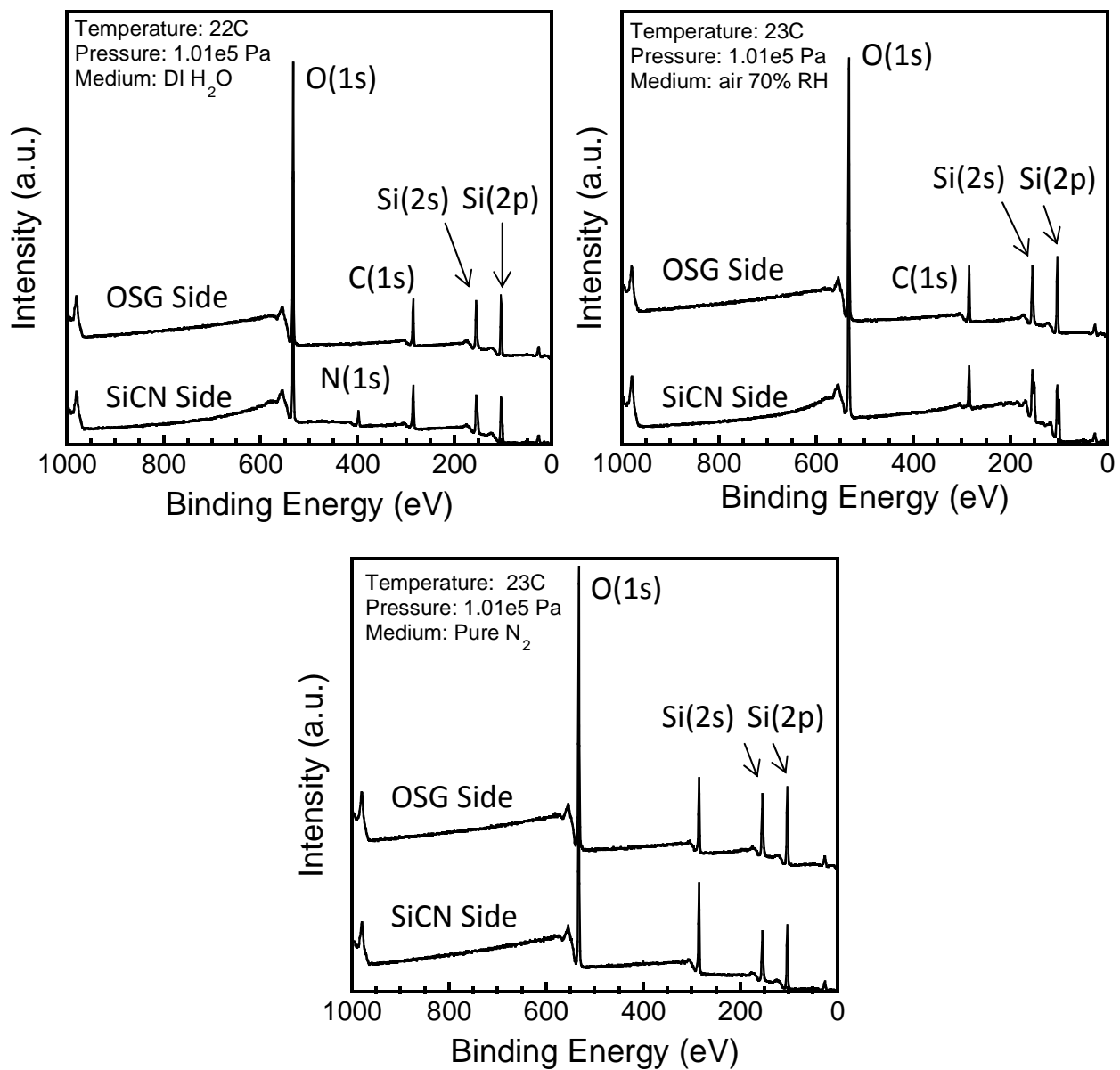


**Figure 4.3. XPS spectra of OSG\_1 samples tested in DI water (top left), air with 70% RH (top right), and pure nitrogen (bottom).**

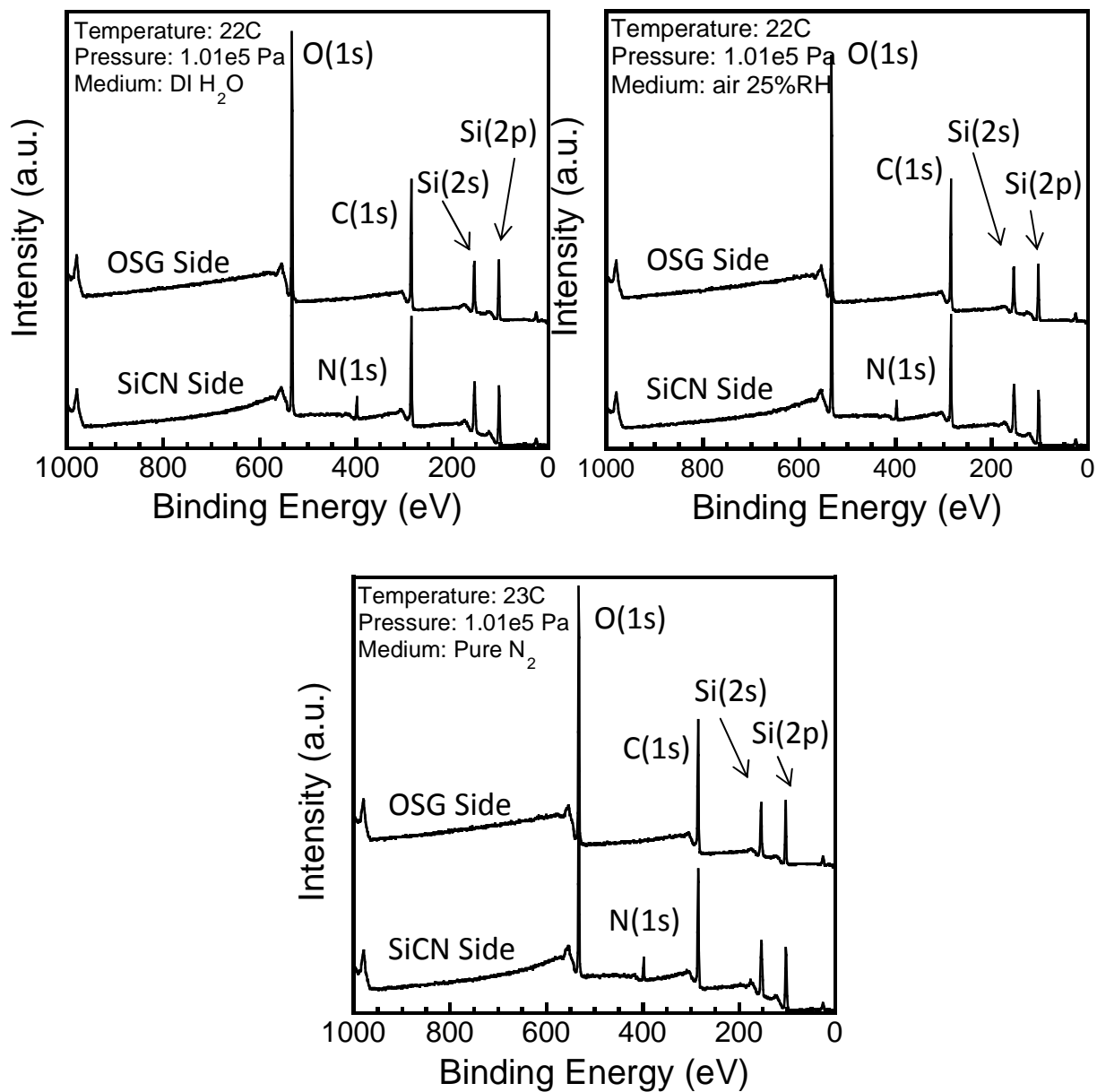
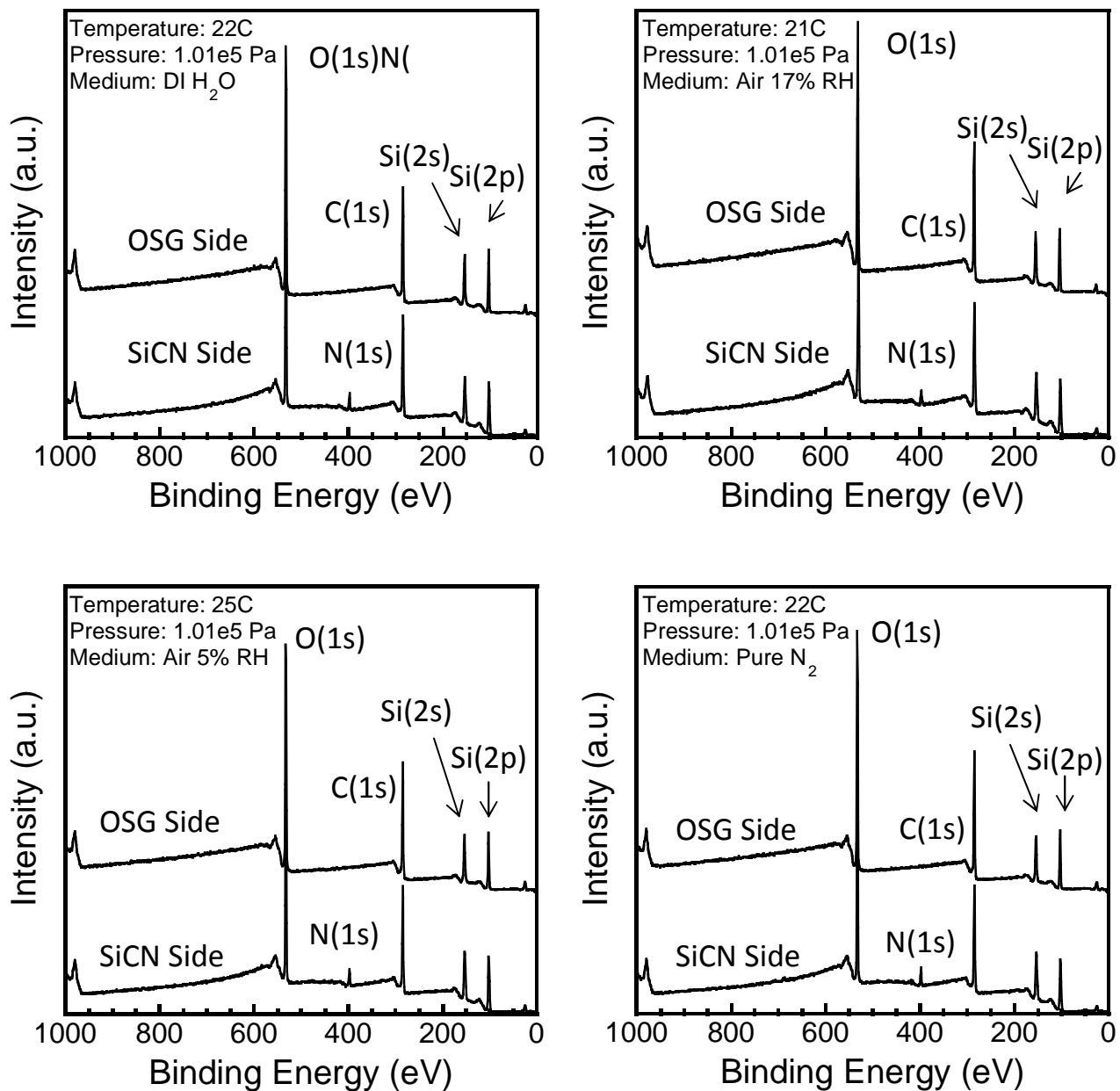


Figure 4.4. XPS spectra of OSG\_2 samples tested in DI water (top left), air with 20% RH (top right), and pure nitrogen (bottom).



**Figure 4.5. XPS spectra of OSG\_3 samples tested in DI water (top left), air with 17% RH (top right), air with 5% RH (bottom left), and pure nitrogen (bottom right).**

**Table 4.2a. Elemental compositions of fractured OSG\_1/SiCN thin film stacks.**

Group	Fractured surfaces	O (%)	C (%)	Si (%)	N (%)
OSG_1-1	Side 1	47.03	21.01	38.64	0.36
	Side 2	42.05	21.34	31.59	5.02
OSG_1-2	Side 1	41.45	18.18	39.97	0.39
	Side 2	43.64	22.46	33.86	0.05
OSG_1-5	Side 1	37.91	34.42	27.51	0.17
	Side 2	40.17	29.23	30.48	0.12
OSG_1-6	Side 1	39.33	19.25	40.93	0.50
	Side 2	42.9	24.00	33.02	0.07

**Table 4.2b. Elemental compositions of fractured OSG\_2/SiCN thin film stacks.**

Group	Fractured surfaces	O (%)	C (%)	Si (%)	N (%)
OSG_2-1	Side 1	33.91	41.37	24.60	0.12
	Side 2	28.78	39.00	28.48	3.73
OSG_2-2	Side 1	28.16	39.37	28.84	3.63
	Side 2	32.51	43.05	24.27	0.17
OSG_2-3	Side 1	27.79	39.53	28.87	3.82
	Side 2	32.69	42.69	24.49	0.12
OSG_2-6	Side 1	28.28	39.43	28.63	3.66
	Side 2	32.75	42.57	24.54	0.14
OSG_2-7	Side 1	28.38	39.38	28.53	3.71
	Side 2	33.13	42.07	24.66	0.13

**Table 4.2c. Elemental compositions of fractured OSG\_3/SiCN thin film composites.**

Group	Fractured surfaces	O (%)	C (%)	Si (%)	N (%)
OSG_3-1	Side 1	34.44	40.05	25.45	0.05
	Side 2	28.52	40.51	27.61	3.35
OSG_3-3	Side 1	27.56	42.34	26.59	3.14
	Side 2	32.09	44.47	23.34	0.10
OSG_3-4	Side 1	27.97	40.09	28.31	3.63
	Side 2	33.01	42.79	24.08	0.12
OSG_3-5	Side 1	27.65	41.28	27.63	3.44
	Side 2	32.39	43.69	23.78	0.14
OSG_3-7	Side 1	29.05	38.94	28.53	3.48
	Side 2	33.74	41.21	24.96	0.09
OSG_3-8	Side 1	27.87	41.46	27.28	3.39
	Side 2	32.62	43.25	23.96	0.14

## 4.2 FRACTURE STRENGTH IN HARSH ENVIRONMENTS

The fracture characteristics of OSG/SiCN specimens in harsh environments, such as high vacuum and low temperature, were also investigated in this research. Table 4.1 shows the detailed testing conditions of all OSG/SiCN samples. They were tested in three different environments: (a) at room temperature and pressure of  $\sim 0.46$  Pa; (b) at room temperature and pressure of  $\sim 1.6 \times 10^{-4}$  Pa; (c) at  $-30$  °C and pressure of  $\sim 0.46$  Pa. The vacuum condition is needed for the low temperature tests to prevent damage caused by ice formation on the linear actuator and other sensitive load cell electronics in the chamber. The results from these experiments are plotted in Figures 4.6 and 4.7. Since the exact water vapor concentration in the chamber was not measured directly during the extreme environment tests, the water partial pressure was assumed to be the same as the chamber pressure. When tested in harsh conditions, the fracture strengths of all three OSG films are very similar to their strengths when tested in pure nitrogen. This is expected because in high vacuum the number of water molecules in the chamber is significantly smaller than in atmospheric conditions. For example, assuming an isothermal system at  $20$  °C and  $101325$  Pa with 100% relative humidity, the water vapor concentration in this enclosed environment is  $5.71 \times 10^{23}$  molecules per meter cubed. According to the ideal gas law, at a pressure of  $1.6 \times 10^{-4}$  Pa, the value used in the harsh environment tests, the vapor concentration drops by  $\sim 9$  orders of magnitude to  $\sim 9.02 \times 10^{14}$  molecules per meter cubed. This reduces the reactant concentration at the crack tip and increases the fracture strength of the OSG/SiCN film stack. In addition, because sticking probability of water to stainless steel 304 increases with decreasing temperature [48, 57], more of the water molecules may attach to the cold chamber wall, further reducing the available reactive species in the testing chamber.

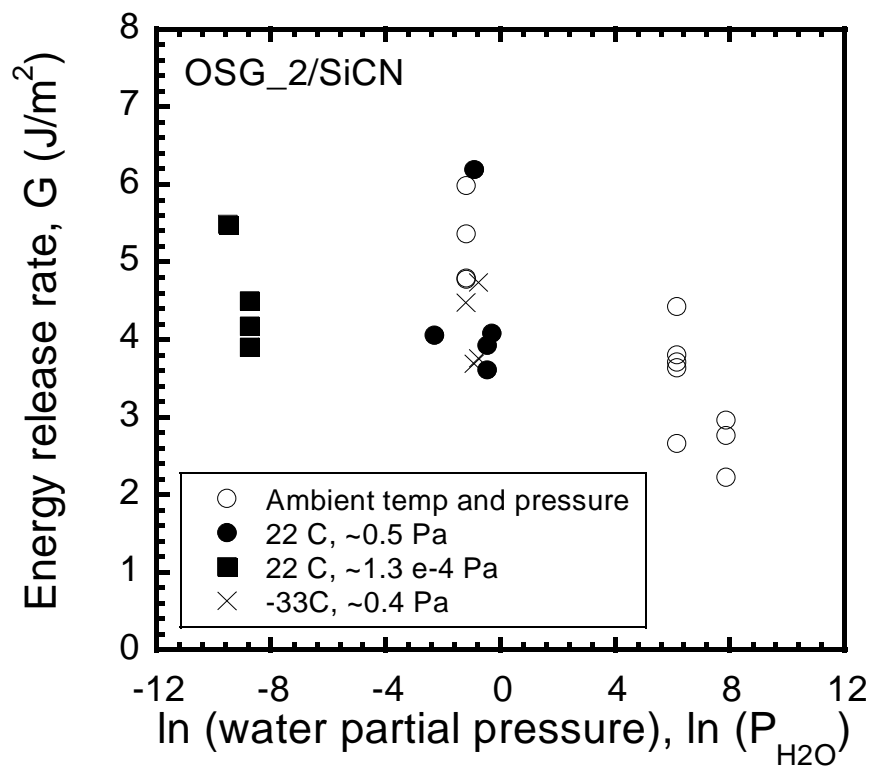


Figure 4.6. Harsh environment performance of OSG\_2.

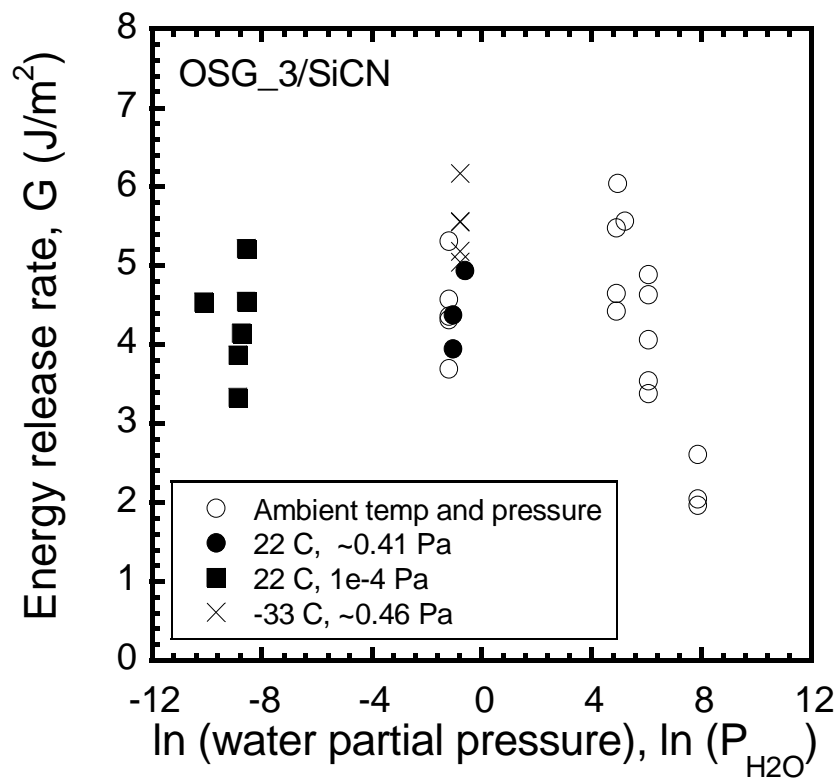
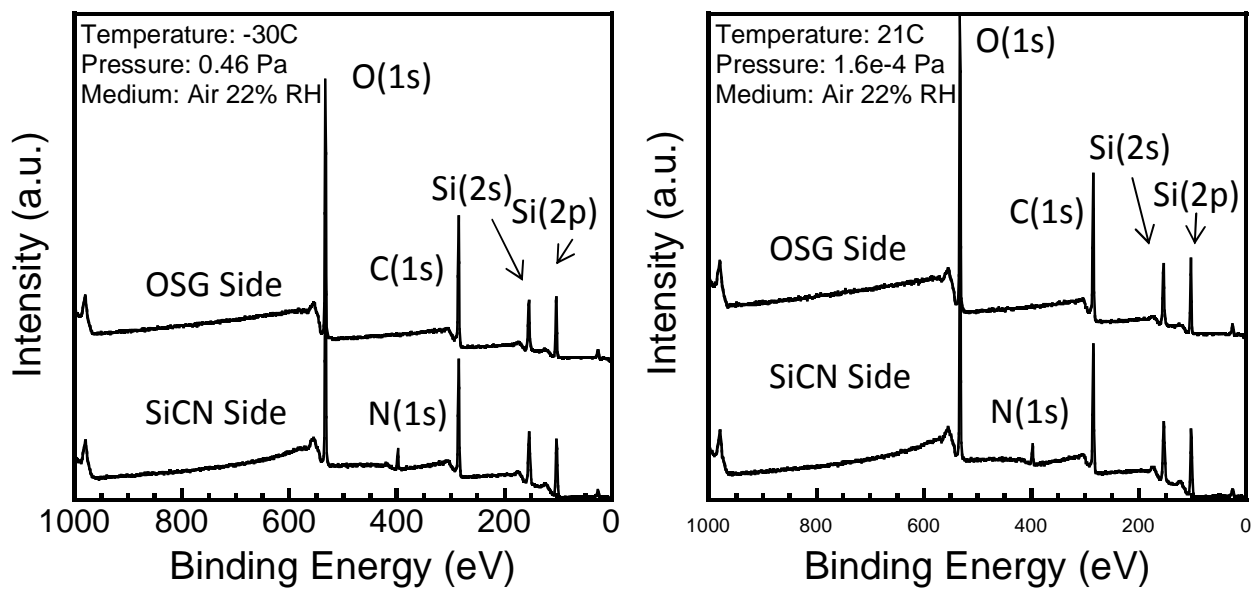


Figure 4.7. Harsh environment performance of OSG\_3.

The XPS spectra from the failed surfaces of the all OSG/SiCN specimens tested at -30 °C and 0.46 Pa are shown in Figures 4.8 and 4.9. Elemental compositions extracted from these spectrums are summarized in Table 4.2. These results reveal that, for each failed specimen, one of the surfaces contains nitrogen peak while the other does not. These are characteristics OSG/SiCN film interface failure. This demonstrates that the fracture behaviors of the OSG\_2 and OSG\_3 are the same in ambient and in the harsh environment.

It is important to note that even though the OSG/SiCN fracture results shown in this work do not indicate a significant temperature or atmospheric pressure sensitivity, other materials may exhibit changes in the fracture behaviors with these environmental parameters. For example, the elastic and plastic properties of some polymeric materials can change with temperature. The results of the FEM experiments described in Section 3.4 show that changes to the release modulus of the epoxy used to create the thin film stacks can lead to changes in fracture energy and mode mix near the crack tip. This emphasizes the importance of harsh environment characterization of these materials in order to design for reliability.



**Figure 4.8. XPS spectra of OSG\_2 samples tested at -30 °C and 0.46 Pa air (top left), and 20 °C and 1.6e-4 Pa air (top right).**

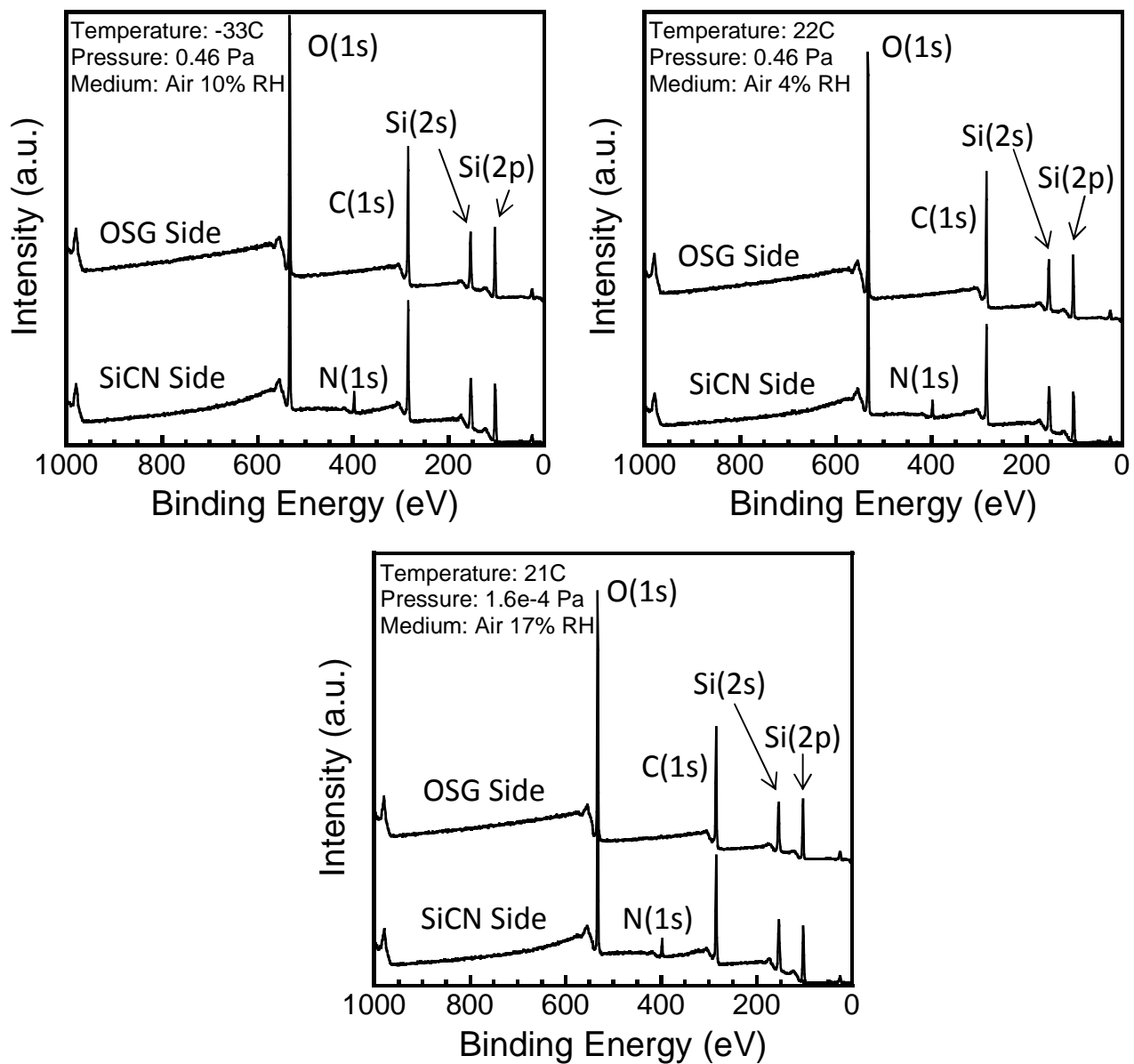


**Figure 4.9.** XPS spectra of OSG\_3 samples tested at -30 °C and 0.46 Pa air (top left), 20 °C and 0.46 Pa air (top right), and 20 °C and 1.4e-4 Pa air (bottom left).

## CHAPTER 5 CONCLUSIONS

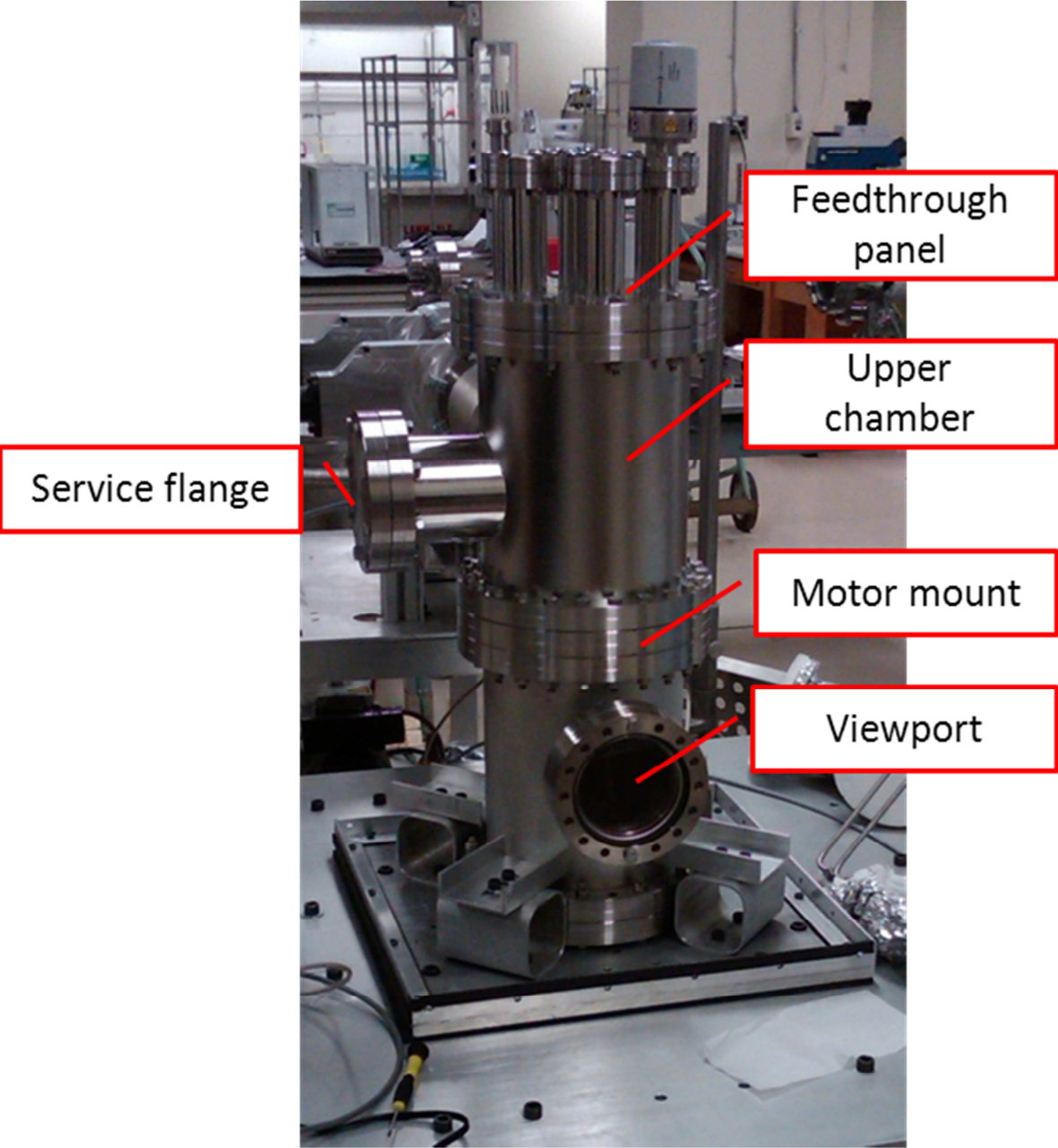
A novel high resolution load and displacement sensing instrument has been constructed with the ability to conduct thin film fracture experiments at temperatures ranging from 20°C to -30 °C and pressure of 1.6e-5 Pa. It is believed that this is the first time that fracture energies of OSG/SiCN films were characterized in low temperature and vacuum environments. The effect of moisture content on the adhesion energy of OSG films with different porosities was investigated. It was observed that the energy release rate was the smallest when samples were submerged in DI water and increased exponentially as moisture concentration was reduced. Porosity was shown to have little effect on the energy release rate of OSG thin films when submerged in DI water. A plateau was observed at 6% RH where the fracture strengths were not significantly different from those obtained in a pure nitrogen environment. Fracture strengths of OSG/SiCN film stacks measured in harsh environments such as low temperature (-30 °C) and high vacuum (4.0e-1 Pa) wear similar to those tested in pure nitrogen gas. This may be explained by the depletion of reactive species in a vacuum and cold environment. XPS results of OSG\_2 and OSG\_3 showed that the cracks propagate through the same interface in ambient and harsh environments.

This research shows that the fracture performance of BEOL dielectrics in extreme environments is critical for IC reliability design. Future work on this topic should include subcritical fracture experiments in order to characterize the fracture velocity of OSG thin films as a function of energy release rate in harsh conditions. The low temperature limits of the test equipment built for this research have not yet been reached and could generate fracture results relevant to aerospace and military applications. Future work should also include characterization

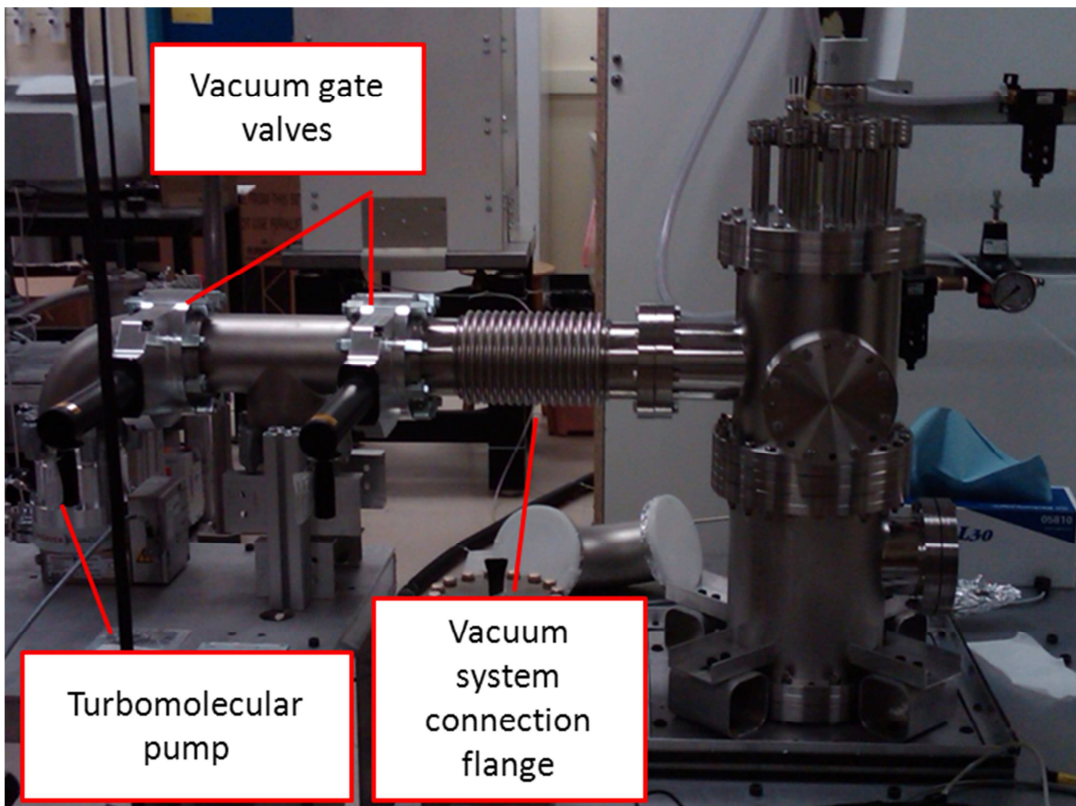
of organic thin films and flexible electronics. Great enthusiasm exists about the future of these technologies and their ability to produce cheap, large scale electronic devices. In OLED's, the anode is usually comprised of transparent conducting oxides such as indium-tin oxide which are typically brittle and have limited flexibility [58]. Careful characterization of the energy release rate of this material will allow for optimization of flexibility and reliability. The finite element model created for this research can also be adapted to simulate the impact of film stack geometry and compliance on the stress intensities created at the crack tip. Different configurations can be generated in order to design for maximum reliability. The effects of plasticity in the film stack can also be simulated with the same model by simply inputting plasticity properties of the stack components.

## APPENDICES

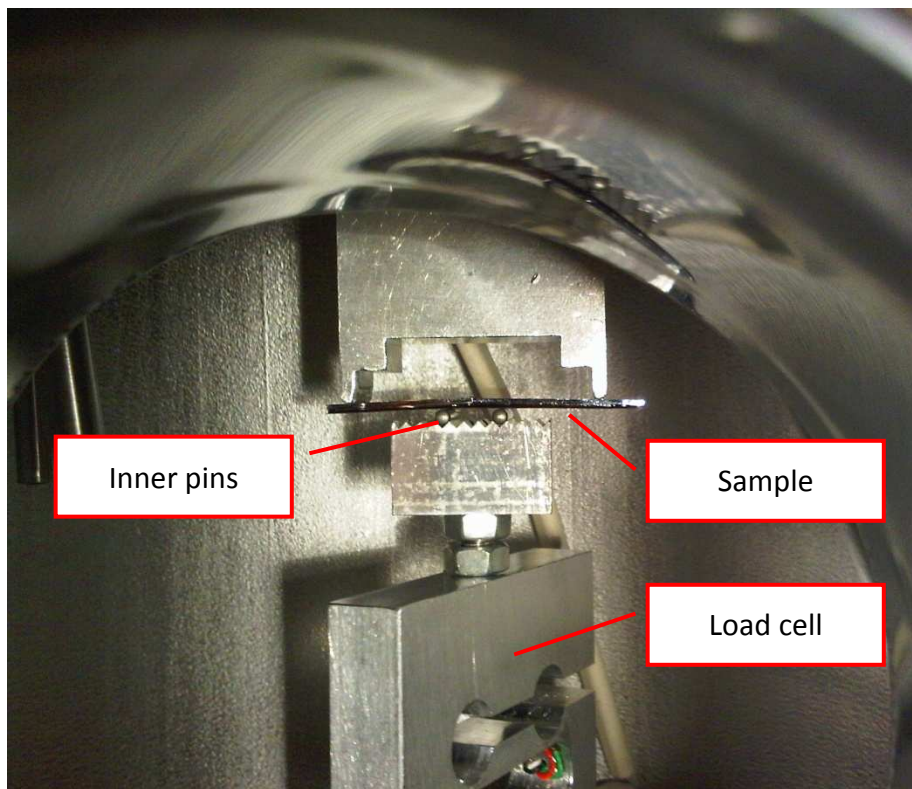
**APPENDIX A. PHOTOGRAPHS OF TEST INSTRUMENT**



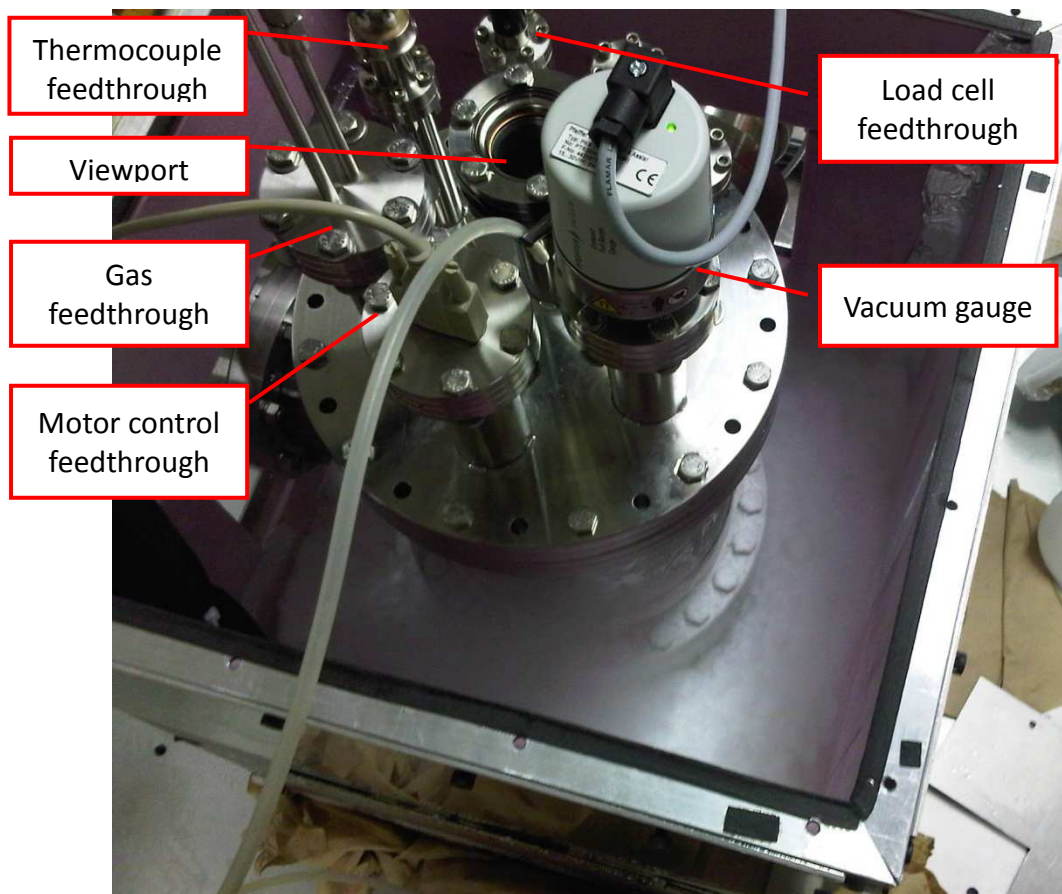
**Photograph of the test instrument with the insulating cage removed.**



**Photograph of the test instrument attached to the dual-stage vacuum system.**



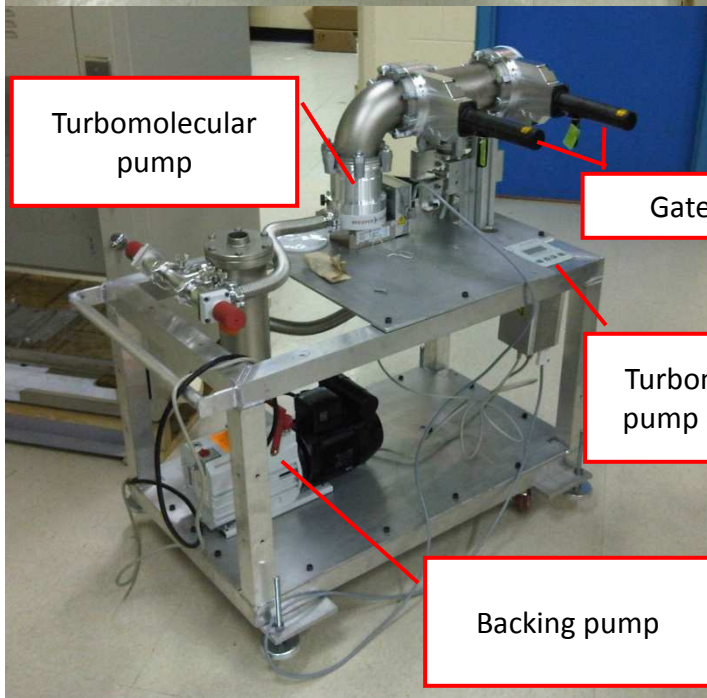
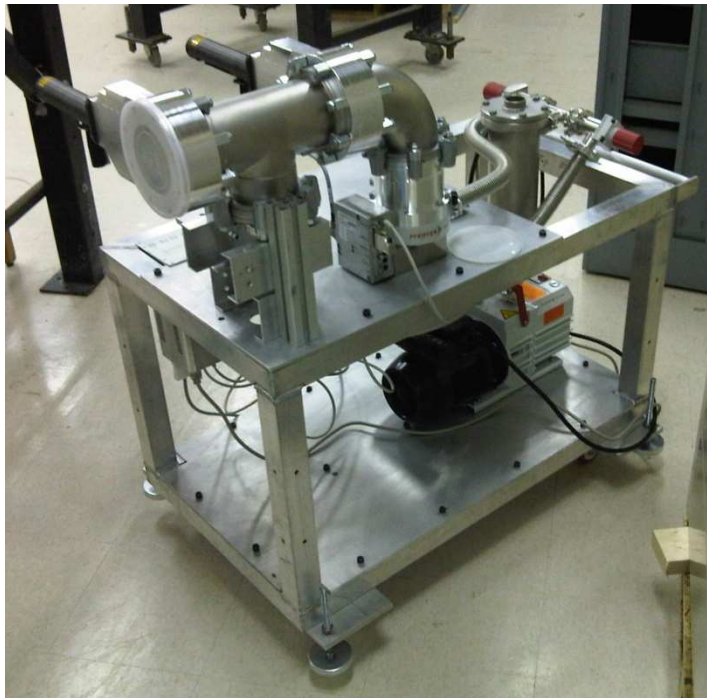
**Close-up photograph through the viewport of the lower chamber. This shows the load cell and four-point bend fixtures. The sample is curved due to the loading conditions.**



**Photograph of the instrument inside the insulating cage. Dry ice is surrounding the lower chamber during a low temperature experiment.**

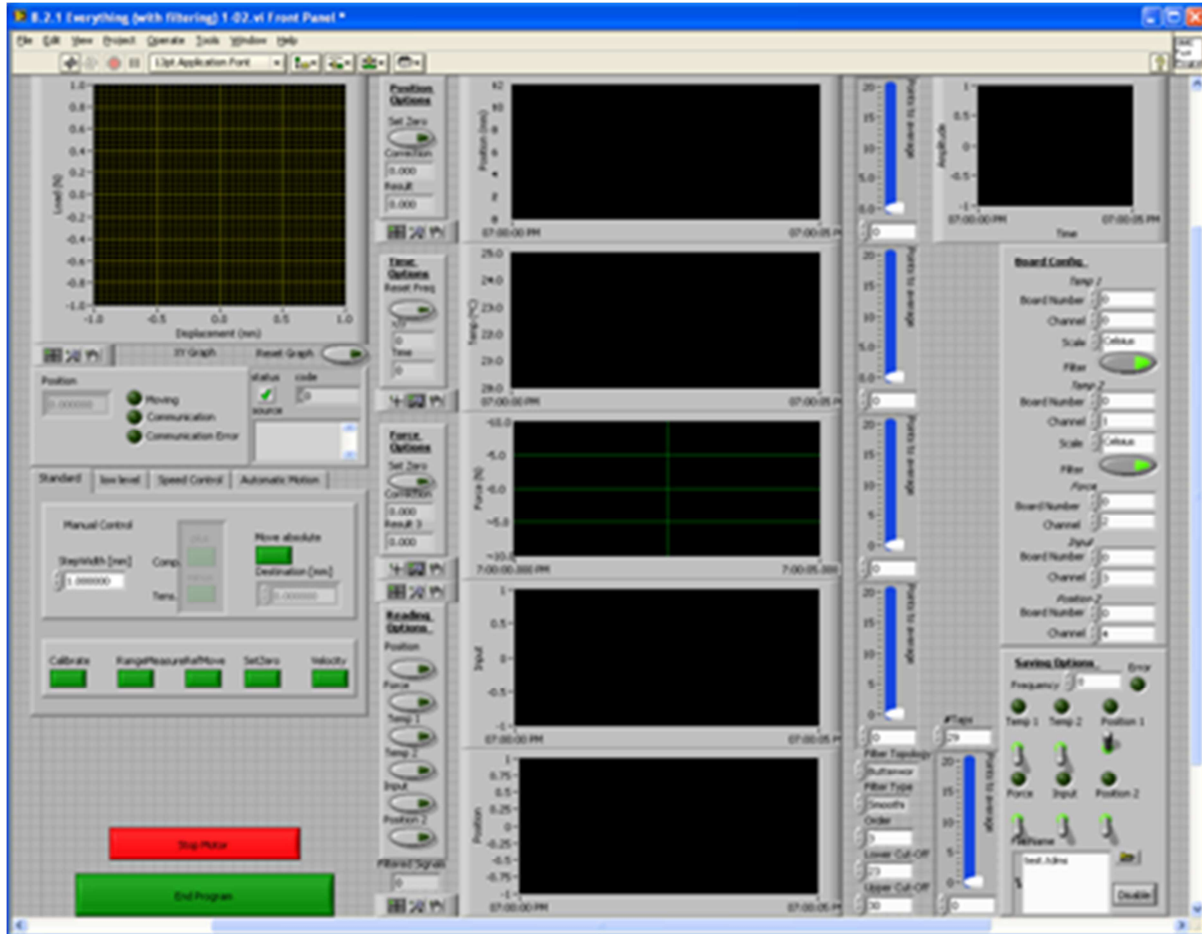


**Photograph of the instrument inside the insulating cage. An access door is opened in order to remove dry ice after a low temperature experiment. A solid flange is used for low temperature tests instead of the sapphire viewport**



**Photographs of the dual-stage vacuum system used in this research. Modular, mobile platform allows this vacuum station to service several chambers in the laboratory. Gate valves allow the turbomolecular pump to be removed from the circuit to and allow the backing pump to operate solo.**

## APPENDIX B. GRAPHIC USER INTERFACE



Screen shot of the graphic user interface (GUI) of the test instrument. The plot in the top left shows the load-displacement curve acquired from a sample. The plots in the center show data obtained from the motor, thermocouples, and load cell with two spare locations for added sensors. The graph on the top right shows the rate of change of force as read by the load cell. Other portions of the GUI allow motor control, file saving, input selection, and filtering.

## BIBLIOGRAPHY

- [1] Cook, R. F., "Mechanical properties of low dielectric-constant organic-inorganic hybrids," in Proceedings of Materials Research Society Symposium, 1999, vol. 576, pp. 301-312.
- [2] Shamiryman, D., Abell, T., Iacopi, F., & Maex, K., "Low-k dielectric materials," Materials today, January 2004, pp. 34-39.
- [3] Iacopi, F., Brongersma, S. H., Vandeveldel, B., O'Toole, M., Degryse, D., Travalay, Y., Maex, K., "Challenges for structural stability of ultra-low-k-based interconnects," Microelectronic Engineering, 2004, vol. 75, pp. 54-62,
- [4] Liu, X. H., Lane, M. W., Shaw, T. M., & Simonyi, E., "Delamination in patterned films," International Journal of Solids and Structures, 2007, vol. 44, pp. 1706-1718.
- [5] Lin, Y., Tsui, T. Y., Vlassak, J., "Octamethylcyclotetrasiloxane-based, low-permittivity Organosilicate coatings," Journal of the Electrochemical Society, 2006, vol. 153, pp.F144-F152.
- [5] Maex, K., Baklanov, M. R., Shamiryman, D., Iacopi, F., Brongersma, S. H., & Yanovitskaya, Z. S., "Low dielectric constant materials for microelectronics," Journal of Applied Physics, 2003, vol. 93, no. 11, pp. 8793-8841.
- [7] O'Neill, M. L., Haas, M. K., Peterson, B. K., Vrtis, R. N., Weigel, S. J., Wu, D. Bitner, M. D., Karwacki, E. J., "Impact of pore size and morphology of porous organosilicate glasses on integrated circuit manufacturing," in Technology and reliability of low-k dielectrics and

- copper interconnects (Materials Research Society Symposium), 2006, vol. 914, Warrendale, PA, , pp. 3-14.
- [8] Morgen, M., Ryan, E. T., Zhao, J. H., Hu, C., Cho, T., & Ho, P. S., "Low dielectric constant materials for ULSI interconnects," Annual Review of Materials Science, 2000, vol. 30, pp. 645-680.
- [9] Li, H., Lin, Y., Tsui, T. Y., & Vlassak, J. J., "The effect of porogen loading on the stiffness and fracture energy of brittle organosilicates," Journal of Materials Research, 2009, vol. 24, no. 1, pp. 107-116.
- [10] Cook, R. F., & Liniger, E. G., "Kinetics of indentation cracking in glass," Journal of the American ceramic society, 1993, pp. 1096-1105.
- [11] Lawn, B. R., "Diffusion-controlled subcritical crack growth in the presence of a dilute gas environment," Materials Science and Engineering, 1974, vol. 13, pp. 277-283.
- [12] Lawn, B. R. "An atomistic model of kinetic crack growth," Journal of Materials Science, 1975, vol. 10, no. 3, pp. 469-480.
- [13] Wiederhorn, S. M., "Influence of water vapour on crack propagation in soda-lime glass," Journal of the American Ceramic Society, 1967, vol. 50, pp. 407-414.
- [14] Wiederhorn, S. M., Fuller, E. R., & Thomson, R., "Micromechanisms of crack growth in ceramics and glasses in corrosive environments," Metal Science, 1980, vol. 14, pp. 450-458.

- [15] Hillig, W. B., & Charles, R. J., "Stress-dependent surface reactions, and strength," in 2nd Proceedings of the High-Strength Materials -- Berkeley International Materials Conference, Berkeley, 1964, pp. 682-705.
- [16] Charles, R. J., "Static fatigue of glass I," *Journal of Applied Physics*, 1958, vol. 29, no. 11, pp. 1549-1553.
- [17] Charles, R. J., "Static fatigue of glass II," *Journal of Applied Physics*, 1958, vol. 29, no. 11, pp. 1554-1560.
- [18] Liniger, E. G., & Cook, R. E., "A controlled flaw technique for lifetime characterization," *Journal of the American Ceramic Society*, 1993, vol. 76, no. 8, pp. 2123-2126.
- [19] Wiederhorn, S. M., & Bolz, L. H., "Stress corrosion and static fatigue of glass," *Journal of the American Ceramic Society*, 1970, vol. 53, no. 10, pp. 543-548.
- [20] Wiederhorn, S. M., & Johnson, H., "Effect of electrolyte pH on crack propagation in glass," *Journal of the American Ceramic Society*, 1973, vol. 56, no. 4, pp. 192-197.
- [21] Wiederhorn, S. M., Johnson, H., Diness, A. M., & Heuer, A. H., "Fracture of Glass in Vacuum," in 75th Annual Meeting of the American Ceramic Society, 1974, vol. 57, Cincinnati, pp. 336-341.
- [22] . Wiederhorn, S. M., & Johnson, H., "Effect of pressure on the fracture of glass," *Journal of Applied Physics*, 1971, vol. 42, no. 2, pp. 681-684.
- [23] Cook, R. F., "Environmentally-controlled non-equilibrium crack propagation in ceramics," *Materials Science and Engineering*, 1999, vol. 260, no. 1-2, pp. 29-40.

- [24] Glasstone, S., Laidler, K. J., & Eyring, H., Theory of rate processes. 1941, New York: McGraw-Hill Book Co.
- [25] Griffith, A. A., "The phenomena of rupture and flow in solids," in Philosophical Transactions of the Royal Society of London, 1921, vol. 221, London, pp. 163-198.
- [26] Irwin, G. R., "Analysis of stresses and strains near the end of a crack traversing a plate," Journal of Applied Mechanics, 1957, vol. 24, pp. 361-364.
- [27] Sneddon, I. N., "The distribution of stress in the neighborhood of a crack in an elastic solid," in The Royal Society of London, Series A, Mathematical and Physical Sciences, 1946, vol. 187, London, pp. 229-260.
- [28] Williams, M. L., "On the stress distribution at the base of a stationary crack," Journal of Applied Mechanics, 1957, vol. 24, pp. 109-114.
- [29] Anderson, T. L., Fracture Mechanics Fundamentals and Applications, vol. 3, 2005, Boca Raton: Taylor and Francis Group.
- [30] Guyer, E. P., Patz, M., & Dauskardt, R. H., "Fracture of nanoporous methyl silsesquioxane thin-film glasses," Journal of Materials Research, 2006, vol. 21, no. 4, pp. 882-894.
- [31] Lin, Y., Xiang, Y., Tsui, T. Y., & Vlassak, J. J., "PECVD low-permittivity organosilicate glass coatings: adhesion, fracture, and mechanical properties," Acta Materialia, 2008, vol. 56, pp. 4932-4943.
- [32] Maidenberg, D. A., Volksen, W., Miller, R. D., & Dauskardt, R. H., "Toughening of nanoporous glasses using porogen residuals," Nature Materials, 2004, vol. 3, pp. 464-469.

- [33] Iacopi, F., Travalay, Y., Eyckens, B., Waldfried, C., Abell, T., Guyer, E. P., Gage, D. M., Dauskardt, R. H., Sajavaara, T., Houthoofd, K., Grobet, P., Jacobs, P., & Maex, K., "Short-ranged structural rearrangement and enhancement of mechanical properties of organosilicate glasses induced by ultraviolet radiation," *Journal of Applied Physics*, 2006, vol. 99, pp. 053511-1 - 053511-7.
- [34] Merrill C. C., & Ho, P. S., "Effect of mode-mixity and porosity on interfacial fracture of low-k dielectrics," in *Technology and Reliability for Advanced Interconnects and Low-k Dielectrics*, 2004, vol. 812, San Francisco, CA, pp. 61-66.
- [35] Cook R. F., & Liniger, E. G., "Stress-corrosion cracking of low-dielectric-constant spin-on-glass thin films," *Journal of Electromechanical Society*, 1999, vol. 146, no. 12, pp. 4439-4448.
- [36] Kook, S.Y. & Dauskardt, R. H., "Moisture-assisted subcritical debonding of a polymer/metal interface," *Journal of Applied Physics*, 2002. vol. 91, no. 3, pp. 1293-1304.
- [37] Lane, M., Dauskardt, R. H., Ma, Q., Fujimoto, H., & Krishna, N., "Subcritical debonding of multilayer interconnect structures: temperature and humidity effects," in *Materials Reliability in Microelectronics IX*, 1999, San Francisco, pp. 263-268.
- [38] Lane, M. W., Snodgrass, J. M., & Dauskardt, R. H., "Environmental effects on interfacial adhesion," *Microelectronics Reliability*, 2001, vol. 41, pp. 1615-1624.
- [39] Hutchinson J. W., & Suo, Z., "Mixed mode cracking in layered materials," *Advances in Applied Mechanics*, 1992, vol. 29, pp. 63-191.

- [40] Liu, X. H., Suo, Z., Ma, Q., & Fujimoto, H., "Developing desing rules to avert cracking and debonding in integrated circuit structures," *Engineering Fracture Mechanics*, 2000, vol. 66, pp. 387-402.
- [41] Vlassak, J. J., "Channel cracking in thin films on substrates of finite thickness," *International Journal of Fracture*, 2003, vol. 119, no. 120, pp. 299-323.
- [42] Vlassak, J. J., Lin, Y., & Tsui, T. Y., "Fracture of organosilicate glass thin films: environmental effects," *Materials Science and Engineering A*, 2005, vol. 391, no. 1-2, pp. 159-174.
- [43] Lin, Y., Tsui, T. Y., & Vlassak, J. J., "Water diffusion and fracture in organosilicate glass film stacks," *Acta Materialia*, 2007, vol. 55, no. 7, pp. 2455-2464.
- [44] Tsui, T. Y., McKerrow, A. J., & Vlassak, J. J., "The effect of water diffusion on the adhesion of organosilicate glass film stacks," *Journal of the Mechanics and Physics of Solids*, 2006, vol. 54, no. 5, pp. 887-903.
- [45] Guyer, E. P., & Dauskardt, R. H., "Effects of solution pH on the accelerated cracking of nanoporous thin-film glasses," *Journal of Materials Research*, 2005, vol. 20, no. 3, pp. 680-687.
- [46] Lin, Y., Vlassak, J. J., Tsui, T. Y., & McKerrow, A. J., "Environmental effects on subcritical delamination of dielectric and metal films from organosilicate glass (OSG) thin films," in *Materials Research Society Symposium*, 2003, vol. 766, pp. 766-771.

- [47] AK steel. AISI Type 304L stainless steel, online, June 20, 2009, <<http://www.matweb.com/search/datasheet.aspx?MatGUID=e2147b8f727343b0b0d51efe02a6127e>>.
- [48] Matos, P. P., McMeeking, R. M., Charalambides, P. G., & Drory, M. D., "A method for calculating stress intensities in bimaterial fracture," *International Journal of Fracture*, 1989, vol. 40, no. 4, pp. 235-254.
- [49] Charalambides, P. G., Cao, H. C., Lund, J., & Evans, A. G., "Development of a test method for measuring the mixed mode fracture resistance of bimaterial interfaces," *Mechanics of Materials*, 1990, vol. 8, no. 4, pp. 269-283.
- [50] Ma, Q., Fujimoto, H., Flinn, P., Jain, V., Adibi-Rizi, F., Moghadam, F. & Dauskardt, R. H., "Quantitative measurement of interface fracture energy in multi-layer thin film structures," 1995, vol. 391, San Francisco, CA, pp. 91-96.
- [51] Ma, Q., "A four-point bending technique for studying subcritical crack growth in thin films and at interfaces," *Journal of Materials Research*, 1997, vol. 12, no. 3, pp. 840-845.
- [52] Dauskardt, R. H., Lane, M., Ma, Q., & Krishna, N., "Adhesion and debonding of multi-layer thin film structures," *Engineering Fracture Mechanics*, 1998, vol. 61, no. 1, pp. 141-162.
- [53] Gage, D. M., Kim, K., Littenken, C. S., & Dauskardt, R. H., "Role of friction and loading parameters in four-point bend adhesion measurements," *Journal of Materials Research*, 2008, vol. 23, no. 1, pp. 87-96.

- [54] Hughey, P. M., Morris, D. J., Cook, R. F., Bozeman, S. P., Kelly, B. L., Chakravarty, S. L. M., Harkens, D. P., & Stearns, L. C., "Four-point bend adhesion measurements of copper and permallow systems," *Engineering Fracture Mechanics*, 2004, vol. 71, pp. 245-261.
- [55] ASTM International, "E1640-09 - Standard test method for assignment of the glass transition temperature by dynamic mechanical analysis," Online, September 12, 2010, <  
[http://enterprise.astm.org/filtrexx.cgi?-P+SUBS\\_COUNT+1+-P+CASTI\\_COUNT+0+-P+DL\\_COUNT+0+-P+CASTI\\_ID++-P+CASTI\\_PASSWORD++-P+COMPANY+University\\_Of\\_Waterloo+-P+ENT\\_COUNT+0+index\\_enterprise\\_fast.frm](http://enterprise.astm.org/filtrexx.cgi?-P+SUBS_COUNT+1+-P+CASTI_COUNT+0+-P+DL_COUNT+0+-P+CASTI_ID++-P+CASTI_PASSWORD++-P+COMPANY+University_Of_Waterloo+-P+ENT_COUNT+0+index_enterprise_fast.frm)>.
- [56] Cao, H. C., & Evans, A. G., "An experimental study of the fracture resistance of bimaterial interfaces," *Mechanics of Materials*, 1989, vol. 7, pp. 295-304.
- [57] Steinherz, H. A., *Handbook of high vacuum engineering*. 1963, New York: Reinhold Publishing Corp.
- [58] Chen, Z., Cotterell, B., & Wang, W., "The fracture of brittle thin films on compliant substrates in flexible displays," *Engineering Fracture Mechanics*, 2002, vol. 69, pp. 597-603.